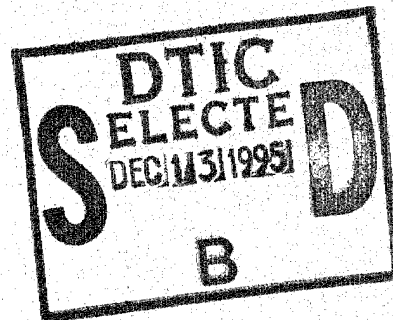


Quarterly Technical Report

Solid State Research



1995:2

Lincoln Laboratory
MASSACHUSETTS INSTITUTE OF TECHNOLOGY
LEXINGTON, MASSACHUSETTS



Prepared for the Department of the Air Force under Contract F19628-95-C-0002.

Approved for public release; distribution is unlimited.

19951211 070

DTIC QUALITY INSPECTED 1

This report is based on studies performed at Lincoln Laboratory, a center for research operated by Massachusetts Institute of Technology. The work was sponsored by the Department of the Air Force under Contract F19628-95-C-0002.

This report may be reproduced to satisfy needs of U.S. Government agencies.

The ESC Public Affairs Office has reviewed this report, and it is releasable to the National Technical Information Service, where it will be available to the general public, including foreign nationals.

This technical report has been reviewed and is approved for publication.

FOR THE COMMANDER


Gary Tutungian
Administrative Contracting Officer
Contracted Support Management

Non-Lincoln Recipients

PLEASE DO NOT RETURN

Permission is given to destroy this document
when it is no longer needed.

MASSACHUSETTS INSTITUTE OF TECHNOLOGY
LINCOLN LABORATORY

SOLID STATE RESEARCH

QUARTERLY TECHNICAL REPORT

1 FEBRUARY-30 APRIL 1995

ISSUED 19 OCTOBER 1995

Approved for public release; distribution is unlimited.

LEXINGTON

MASSACHUSETTS

ABSTRACT

This report covers in detail the research work of the Solid State Division at Lincoln Laboratory for the period 1 February through 30 April 1995. The topics covered are Electrooptical Devices, Quantum Electronics, Materials Research, Submicrometer Technology, High Speed Electronics, Microelectronics, and Analog Device Technology. Funding is provided primarily by the Air Force, with additional support provided by the Army, ARPA, Navy, BMDO, NASA, and NIST.

Accession For	
NTIS GRA&I	<input checked="checked" type="checkbox"/>
DTIC TAB	<input type="checkbox"/>
Unannounced	<input type="checkbox"/>
Justification	
By	
Distribution/	
Availability Codes	
Dist	Avail and/or Special
A-1	

TABLE OF CONTENTS

Abstract	iii
List of Illustrations	vii
List of Tables	ix
Introduction	xi
Reports on Solid State Research	xiii
Organization	xxiii
 1. ELECTROOPTICAL DEVICES	 1
1.1 Relative Intensity Noise of High-Power 1.3- μ m InGaAsP/InP Tapered Diode Amplifiers	 1
 2. QUANTUM ELECTRONICS	 3
2.1 Calorimetric Measurement of Losses in 193-nm Optics	3
 3. MATERIALS RESEARCH	 7
3.1 InAsSb/InAlAsSb Strained Quantum-Well Diode Lasers Emitting at 3.9 μ m	7
3.2 <i>n</i> -AlGaSb and GaSb/AlGaSb Double-Heterostructure Lasers Grown by Organometallic Vapor Phase Epitaxy	10
3.3 Reactor Design for In-Situ Optical Monitoring of Chemical Vapor Deposition Reactors	13
 4. SUBMICROMETER TECHNOLOGY	 21
4.1 Optimization of a 193-nm Silylation Process for Sub-0.25- μ m Lithography	21
 5. HIGH SPEED ELECTRONICS	 27
5.1 Fabrication and Microwave Characterization of Thin-Film PZT Capacitors	27
 6. MICROELECTRONICS	 31
6.1 Charge-Coupled-Device Detection of Micro Dispensed DNA Hybridization Arrays	31
6.2 First Imaging Tests of Wafer-Scale Charge-Coupled-Device Imager	34
 7. ANALOG DEVICE TECHNOLOGY	 37
7.1 Microwave Filters Made from High-Temperature Superconductors with High-Power-Handling Capability	37

LIST OF ILLUSTRATIONS

Figure No.		Page
1-1	Schematic diagram of experimental configuration showing tapered amplifier device injected with light from diode-pumped Nd:YAG laser.	1
1-2	Measured relative intensity noise (RIN) spectrum of tapered amplifier operating at 1319 nm with output power of 360 mW.	2
2-1	Setup for absorption measurements.	3
2-2	Flow through thermoelectric module as a function of time.	4
3-1	Calculated conduction- and valence-band offsets between $\text{InAs}_{0.85}\text{Sb}_{0.15}$ and InAlAsSb with fixed tensile strain of 5×10^{-3} as a function of Al content.	8
3-2	Pulsed threshold current density vs temperature of $100 \times 1000\text{-}\mu\text{m}$ strained quantum-well (QW) laser. Data for the best double-heterostructure (DH) laser at $3.9 \mu\text{m}$ are shown for comparison.	8
3-3	CW power vs current of $100 \times 1000\text{-}\mu\text{m}$ device at several temperatures.	9
3-4	Electron concentration of Te-doped GaSb and $\text{Al}_{0.4}\text{Ga}_{0.6}\text{Sb}$ as a function of DETe mole fraction.	11
3-5	Room-temperature electron concentration and mobility of Te-doped $\text{Al}_x\text{Ga}_{1-x}\text{Sb}$.	11
3-6	Carbon, tellurium, and oxygen levels in Te-doped $\text{Al}_x\text{Ga}_{1-x}\text{Sb}$ layers measured by secondary ion mass spectrometry.	12
3-7	Pulsed power vs current for $100 \times 500\text{-}\mu\text{m}$ GaSb/AlGaSb DH laser emitting at $1.75 \mu\text{m}$. Inset shows I-V curve.	12
3-8	Vertical rotating-disk reactor design with top optical access for Raman scattering measurements.	14
3-9	Flow patterns for (a) 1.27-cm-radius and (b) 2.54-cm-radius optical windows. The susceptor rotation rate is 400 rpm.	15
3-10	Double-crystal x-ray diffraction curves at three locations on wafer radius, showing high layer uniformity.	16
3-11	Vertical rotating-disk reactor design with side optical access for spectroscopic ellipsometry.	17
3-12	Flow visualization in reactor tube with modifications for in-situ monitoring by Raman scattering and spectroscopic ellipsometry.	18

LIST OF ILLUSTRATIONS (Continued)

Figure No.		Page
4-1	Schematic process flow for positive-tone 193-nm silylation process.	21
4-2	Silylation process linearity at best dose (100 dose units, $\sim 100 \text{ mJ/cm}^2$). The resist, 0.76- μm -thick polyvinylphenol (PVP) silylated with dimethylsilyldimethylamine (DMSDMA) at 90°C and 25 Torr for 60 s, was etched under optimized conditions (see Table 4-1) with a 100% overetch. The grating linearity is extended to 0.175 μm for a 30-s silylation time and 25% overetch. The two solid lines are the acceptable performance, i.e., $\pm 10\%$ deviations from the nominal feature size.	23
4-3	Total exposure latitude vs feature size for gratings ($\pm 10\%$ critical dimension). The resist, 0.76- μm -thick PVP silylated with DMSDMA at 90°C and 25 Torr for 30 and 60 s, was etched under optimized conditions (see Table 4-1) with a 25% overetch.	24
4-4	Experimental exposure-dose matrix for 0.25-, 0.20-, and 0.175- μm gratings ($\pm 10\%$ critical dimension). Each 193-nm dose unit corresponds to $\sim 1 \text{ mJ/cm}^2$. The resist, 0.50- μm -thick PVP silylated with DMSDMA at 90°C and 25 Torr for 30 s, was etched under optimized conditions (see Table 4-1) with a 25% overetch.	25
4-5	Scanning electron micrograph of 0.20- μm silylated resist features. The resist, 0.76- μm -thick PVP silylated with DMSDMA at 90°C and 25 Torr for 60 s, was etched under optimized conditions (see Table 4-1) with a 100% overetch.	26
5-1	Top view of microwave coplanar waveguide structure for ferroelectric test chip.	28
6-1	Two-dimensional images formed by x-ray film and 420×420 -pixel charge-coupled-device (CCD) imager after exposure to radioisotope-labeled hybridized array.	32
6-2	Sequences used in micro dispensed hybridization experiment. Target sequence has ^{35}S on 5' terminus. Probes were linked to glass substrates through their 3' terminus employing epoxysilane chemistry and an amino linkage as previously described in Ref. 6.	33
6-3	(a) Top and (b) cross-sectional views illustrating the placement of the carrier substrate containing the DNA samples relative to the CCD detector for proximity imaging of the beta particle emission.	33
6-4	Video image obtained from 1960×2560 -pixel CCD imager.	35
6-5	Expanded view of portion of image of Figure 6-4 containing plaque mounted on right side of house.	35

LIST OF ILLUSTRATIONS (Continued)

Figure No.		Page
6-6	Test results on 32×32 -pixel imager located at edge of same chip as the large device and operated at 1000 frames/s. A pulsed light-emitting diode, pinhole, and lens are used to illuminate a small region of the device, and three frames of the output video are shown.	36
7-1	Photograph of high-temperature superconductive microwave filter built using thin films of yttrium-barium-copper oxide deposited on LaAlO_3 . The substrate is soldered to the package to ensure good thermal contact at low temperatures.	37
7-2	Variation of Q of 10- Ω microstrip resonator with peak RF current in the resonator. Measurements were made at 50 K.	38
7-3	Calculated rms current in (a) resonators 1, 2, and 3 and (b) resonators 4 and 5 as a function of frequency for 1-W input to filter.	39
7-4	Calculated and measured insertion loss for filter of Figure 7-1. The calculations are based on Q measurements at 50 K. The insertion loss was measured at 45 K with a single-tone signal at the center of the band.	40
7-5	Measured frequency response of the filter as a function of the input power at 58 K.	41

LIST OF TABLES

Table No.		Page
4-1	Silylation Process Parameters in Sub-0.25- μm Lithography	24
5-1	Voltage Dependence of Electrical Properties of 0.5- μm Thin-Film PZT at 5 GHz	29

INTRODUCTION

1. ELECTROOPTICAL DEVICES

The relative intensity noise of high-power 1.3- μm InGaAsP/InP tapered diode amplifiers has been measured to be as low as -164 dB/Hz at 360-mW output power. These low-noise lasers are attractive for wide-dynamic-range analog optical link applications.

2. QUANTUM ELECTRONICS

Losses of fused silica samples from various sources have been measured by a calorimetric technique at the ArF excimer laser wavelength of 193 nm, utilizing a thermoelectric module as a heat flow detector: the detector signal is directly calibrated in watts, independent of the geometry and thermal properties of the sample being tested. A sensitivity of fractional milliwatts was easily obtained, allowing measurement of losses in the few-percent range with a 0.1% resolution, and separation of the measured loss between absorption and scattering was achieved by appropriately changing the optical configuration of the samples.

3. MATERIALS RESEARCH

Strained quantum-well diode lasers consisting of compressively strained InAsSb active layers and tensile-strained InAlAsSb barrier layers have exhibited pulsed operation up to 165 K, with a threshold current density of 78 A/cm^2 at 80 K. The devices operated CW up to 123 K, and the maximum CW power at 80 K was 30 mA/facet.

N-type doping of AlGaSb epilayers grown by organometallic vapor phase epitaxy (OMVPE) has been achieved for the first time. Lattice-mismatched double-heterostructure diode lasers with AlGaSb cladding layers and a GaSb active layer were demonstrated, indicating the potential of OMVPE for growth of GaSb-based materials for electronic and optoelectronic devices.

A reactor that permits in-situ optical monitoring of chemical vapor deposition growth in a vertical rotating-disk reactor has been designed. Surface Raman spectroscopy and spectroscopic ellipsometry can be performed without affecting epitaxial growth uniformity.

4. SUBMICROMETER TECHNOLOGY

A positive-tone silylation resist process has been optimized for use with 193-nm optical lithography. Vertical resist profiles, large exposure and defocus latitudes, and good feature size linearity were demonstrated.

5. HIGH SPEED ELECTRONICS

Measurements performed on thin-film ferroelectric capacitors made from lead zirconium titanate (PZT) have shown that the PZT retains a very high dielectric constant up to 15 GHz. The capacitors meet the need for very small devices with the highest possible capacitance values, such as on the multichip module being developed for ultra-high-speed electronic systems, which requires decoupling capacitors to suppress the current surges in the power supply lines.

6. MICROELECTRONICS

Charge-coupled devices (CCDs) have been shown experimentally to be efficient detectors of the radioisotope label ^{35}S present in micro dispensed sites of hybridized DNA. Sensitive detection of micro dispensed nucleic acids is needed for automating the method of DNA sequencing by hybridization.

Large 1960×2560 -pixel wafer-scale CCD imaging devices have been produced with very low cosmetic defect counts, and in first tests have yielded excellent high-resolution imagery. The 32×32 -pixel photometers on the same device have been successfully operated at the design-goal rate of 1000 frames/s.

7. ANALOG DEVICE TECHNOLOGY

Microwave filters with high-power-handling capabilities have been built using high-transition-temperature superconducting thin films. Nonlinear circuit analysis has been used successfully to predict the filter response.

REPORTS ON SOLID STATE RESEARCH

1 FEBRUARY THROUGH 30 APRIL 1995

PUBLICATIONS

High-Performance 770-nm AlGaAs-GaAsP Tensile-Strained Quantum-Well Laser Diodes	F. Agahi* K. M. Lau* H. K. Choi A. Baliga* N. G. Anderson*	<i>IEEE Photon. Technol. Lett.</i> 7 , 140 (1995)
Low-Power Adaptive Filter	A. M. Chiang	<i>1994 Government Microcircuit Applications Conference Digest of Papers</i> , Vol. 20, p. 557
GaSb-Based Mid-Infrared Quantum-Well Diode Lasers	H. K. Choi G. W. Turner	<i>Proc. SPIE</i> 2382 , 236 (1995)
High-Power, High-Temperature Operation of GaInAsSb-AlGaAsSb Ridge-Waveguide Lasers Emitting at 1.9 μm	H. K. Choi G. W. Turner M. K. Connors S. Fox* C. Dauga* M. Dagenais*	<i>IEEE Photon. Technol. Lett.</i> 7 , 281 (1995)
Specific Contact Resistance Measurements of Ohmic Contacts to Semiconducting Diamond	C. A. Hewett* M. J. Taylor J. R. Zeidler* M. W. Geis	<i>J. Appl. Phys.</i> 77 , 755 (1995)
Preshaping Photoresist for Refractive Microlens Fabrication	T. R. Jay M. B. Stern	<i>Opt. Eng.</i> 33 , 3552 (1994)

*Author not at Lincoln Laboratory.

Pulsed Anodization Techniques for Fabricating GaSb-Based Lasers	C. C. Largent* M. J. Grove* P. S. Zory* H. K. Choi G. W. Turner	<i>Proc. SPIE</i> 2382 , 244 (1995)
Microwave Hysteretic Losses in $\text{YBa}_2\text{Cu}_3\text{O}_{7-x}$ and NbN Thin Films	P. P. Nguyen* D. E. Oates G. Dresselhaus* M. S. Dresselhaus* A. C. Anderson	<i>Phys. Rev. B</i> 51 , 6686 (1995)
193 nm — Moderately Extreme Ultraviolet	M. Rothschild	<i>OSA Proc.</i> 23 , 10 (1994)
Dry Etching for Coherent Refractive Microlens Arrays	M. B. Stern T. R. Jay	<i>Opt. Eng.</i> 33 , 3547 (1994)
Heterodyne Nondegenerate Pump-Probe Measurement Technique for Guided-Wave Devices	C.-K. Sun* B. Golubovic* J. G. Fujimoto* H. K. Choi C. A. Wang	<i>Opt. Lett.</i> 20 , 210 (1995)
Growth of InAsSb Quantum Wells for Long-Wavelength ($\sim 4\ \mu\text{m}$) Lasers	G. W. Turner H. K. Choi H. Q. Le	<i>J. Vac. Sci. Technol. B</i> 13 , 699 (1995)
Coupled-Davity Electro-optically Q-Switched Nd:YVO ₄ Microchip Lasers	J. J. Zayhowski C. Dill III	<i>Opt. Lett.</i> 20 , 716 (1995)
Tm:YVO ₄ Microchip Laser	J. J. Zayhowski J. Harrison* C. Dill III J. Ochoa	<i>Appl. Opt.</i> 34 , 435 (1995)

*Author not at Lincoln Laboratory.

ACCEPTED FOR PUBLICATION

N-Type III-V Multiple-Quantum-Well Detectors Exhibiting Normal-Incidence Response	E. R. Brown S. J. Eglash K. A. McIntosh	<i>In III-V Semiconductor Quantum Wells and Superlattices for Long Wavelength Infrared Detectors</i> , M. Razeghi, ed. (Gordon & Breach, Newark, N.J.)
InAsSb/InAlAsSb Strained Quantum-Well Diode Lasers Emitting at 3.9 μm	H. K. Choi G.W. Turner	<i>Appl. Phys. Lett.</i>
InAsSb/InAlAsSb Strained Quantum-Well Lasers Emitting at 4.5 μm	H. K. Choi G.W. Turner H. Q. Le	<i>Appl. Phys. Lett.</i>
Basic Module for an Integrated Optical Phase Difference Measurement and Correction System	B. Golubovic* J. P. Donnelly C. A. Wang W. D. Goodhue R. H. Rediker*	<i>IEEE Photon. Technol. Lett.</i>
193-nm Lithography at MIT Lincoln Laboratory	M. S. Hibbs* R. R. Kunz M. Rothschild	<i>Solid State Technol.</i>
Polymers for Microelectronics	R. R. Kunz	<i>In American Institute of Physics Handbook for Polymers</i> , J. E. Mark, ed. (AIP Press, Woodbury, N.Y.)
Uniform Linear Arrays of Strained-Layer InGaAs/AlGaAs Quantum-Well Ridge-Waveguide Diode Lasers Fabricated by ECR-IBAE	J. D. Woodhouse C. A. Wang J. P. Donnelly D. Z. Tsang R. J. Bailey D. E. Mull K. Rauschenbach	<i>J. Quantum Electron.</i>

*Author not at Lincoln Laboratory.

PRESENTATIONS[†]

Spectroscopy and Diode-Pumped Lasing of Yb ³⁺ -Doped Lu ₃ Al ₅ O ₁₂ (Yb:LuAG)	T. Y. Fan D. S. Sumida*	} Advanced Solid-State Lasers Meeting, Memphis, Tennessee, 29 January–1 February 1995
Radiation Trapping in Solid State Laser Media and Its Impact on Fluorescence Lifetime and Emission Cross Section Measurements	D. S. Sumida* T. Y. Fan	
High-Power Diode-Pumped Mid- Infrared Semiconductor Lasers	H. Q. Le G. W. Turner J. R. Ochoa H. K. Choi J. M. Arias* M. Zandian* R. Zucca* Y.-Z. Liu	} Photonics West '95, San Jose, California, 4-10 February 1995
GaSb-Based Mid-Infrared Diode Lasers	H. K. Choi G. W. Turner	
Pulsed Anodization Technique for Fabricating GaSb-Based Lasers	C. C. Largent* M. J. Grove* P. S. Zory* H. K. Choi G. W. Turner	
Mass-Transport Fabrication of Large- Numerical-Aperture Microoptics	Z. L. Liao	SPIE's OE/LASE '95, San Jose, California, 6-10 February 1995
GaSb-Based Mid Infrared Semiconductor Lasers	H. K. Choi	Technical Seminar, Stanford University, Stanford, California, 10 February 1995

*Author not at Lincoln Laboratory.

[†]Titles of presentations are listed for information only. No copies are available for distribution.

Diamond Field-Emission Cathodes

M. W. Geis
J. C. Twichell
M. B. Stern
N. N. Efremow
K. E. Krohn
T. M. Lyszczarz
R. Uttaro

Electrical Engineering and
Computer Science Colloquium,
Cambridge, Massachusetts,
13 February 1995

Integrated Optics

L. M. Johnson

Lincoln Laboratory
Technical Seminar Series,
University of Colorado,
Fort Collins, Colorado,
16 February 1995

193 nm Single Laser Positive Resists:
Building Etch Resistance into a High
Resolution Imaging System

R. D. Allen*
G. M. Wallraff*
R. A. DiPietro*
D. C. Hofer*
R. R. Kunz

The 193-nm Full-Field Step-and-Scan
Prototype at MIT Lincoln Laboratory

M. S. Hibbs*
R. R. Kunz
M. Rothschild

All-Dry Resist Processes for 193-nm
Lithography

M. W. Horn
B. E. Maxwell
R. R. Kunz
M. S. Hibbs*
S. C. Palmateer
A. R. Forte

SPIE Symposium on
Microlithography '95,
Santa Clara, California,
19-24 February 1995

Optimization of a 193-nm Silylation Process
for Sub-0.25- μ m Lithography

S. C. Palmateer
R. R. Kunz
A. R. Forte

Applications of Plasma Polymerized
Methylsilane Resist for All Dry 193-nm
Deep UV Lithography

T. W. Weldman*
R. Kostelak*
S. Vaidya*
O. Joubert*
S. C. Palmateer
M. S. Hibbs*

*Author not at Lincoln Laboratory.

Superconducting Filter Design with Simulators: Issues and Techniques	W. G. Lyons	Meeting of the Boston Chapter, IEEE Microwave Theory and Techniques Society, Burlington, Massachusetts, 21 February 1995
Integrated Optical Guided-Wave Components and Devices in AlGaAs/GaAs and InGaAsP/InP	J. P. Donnelly	Lincoln Laboratory Technical Seminar Series, University of Illinois, Urbana, Illinois, 23 February 1995
Optical Link for Cellular Telephone Microcells	G. E. Betts	Optical Fiber Communications, San Diego, California, 27 February–2 March 1995
Oil Thickness Detection Using Wideband Radiometry	O. B. McMahon E. R. Brown G. M. Daniels T. J. Murphy G. Hover*	1995 International Oil Spill Conference, Long Beach, California, 27 February–2 March 1995
Materials Evaluation of Antireflective Coatings for Single-Layer 193-nm Lithography	R. R. Kunz R. D. Allen*	248/193-nm Process Window Workshop, Austin, Texas, 9-10 March 1995
Optimization of a 193-nm Silylation Process for Sub-0.25- μ m Lithography	S. C. Palmateer R. R. Kunz A. R. Forte	
A Comparison Between Aerial Images at 248 and 193 nm for Sub-0.25- μ m Features	M. Rothschild S. P. Doran E. Barouch* U. Hollerbach*	
High-Density 300 Gbps/cm ² Parallel Free-Space Optical Interconnection Design Considerations	D. Z. Tsang	Spring Topical Meetings, Salt Lake City, Utah, 12-17 March 1995

*Author not at Lincoln Laboratory.

Ultrafast Low-Temperature-Grown
GaAs Photomixers

K. A. McIntosh
E. R. Brown
K. B. Nichols
O. B. McMahon
K. M. Molvar
W. F. DiNatale
T. M. Lyszczarz

Ultrafast Electronics and
Optoelectronics,
Dana Point, California,
13-17 March 1995

Microwave Vortex Dynamics in the
Random Pinning Potential of
 $\text{YBa}_2\text{Cu}_3\text{O}_{7-x}$

N. R. Belk*
D. E. Oates
G. Dresselhaus*
M. S. Dresselhaus*
A. C. Anderson

Microwave and Millimeter-Wave
Applications of Photonic Crystals

E. R. Brown

March Meeting of American
Physical Society,
San Jose, California,
20-24 March 1995

Microwave Power Dependence of
 $\text{YBa}_2\text{Cu}_3\text{O}_{7-x}$ Thin-Film Josephson
Edge Junctions

D. E. Oates
P. P. Nguyen*
Y. Habib*
M. S. Dresselhaus*
G. Dresselhaus*
G. Koren*
E. Polturak*

Microchip Lasers

J. J. Zayhowski

Lincoln Laboratory
Technical Seminar Series,
Purdue University,
Lafayette, Indiana,
21 March 1995;
Northwestern University,
Evanston, Illinois,
6 April 1995

*Author not at Lincoln Laboratory.

In-Situ FTIR Monitoring of
Organometallic Concentration in
OMCVD Reactor

Tritertiarybutylaluminum as a Novel
Precursor for III-V Alloys

Top-Surface Imaged Resist Processes
for 193-nm Lithography

The Role of Impurities in Hydride
Vapor Phase Epitaxy Grown Gallium
Nitride

High-Power Microwave Devices:
How Far Can Thin Films Go?

Back-Illuminated Wafer-Scale
CCD Imager

C. A. Wang
S. Salim*
R. D. Driver*
K. F. Jensen*

C. A. Wang
S. Salim*
K. F. Jensen*
A. C. Jones*

R. R. Kunz
S. C. Palmateer
A. R. Forte
M. W. Horn

R. J. Molnar
K. B. Nichols
E. R. Brown
I. Melngailis

D. E. Oates
A. C. Anderson

B. E. Burke
J. A. Gregory
R. W. Mountain
B. B. Kosicki
H. C. Clark
P. J. Daniels
V. S. Dolat
T. L. Lind
T. C. Hotaling
A. H. Loomis
D. J. Young

7th Biennial Workshop on
Organometallic Vapor Phase
Epitaxy,
Fort Myers, Florida,
2-6 April 1995

American Chemical Society
National Symposium,
Anaheim, California,
2-7 April 1995

1995 Spring Materials Research
Society Meeting,
San Francisco, California,
17-21 April 1995

1995 IEEE Workshop on CCDs
and Advanced Image Sensors,
Dana Point, California,
20-22 April 1995

*Author not at Lincoln Laboratory.

Progress in 4- μ m Quantum-Well
Diode Lasers

H. K. Choi
G. W. Turner

Status of Diode-Pumped Mid-Infrared
Semiconductor Lasers

H. Q. Le
G. W. Turner
H. K. Choi
A. Sanchez

8th Annual Diode Laser
Technology Conference,
Fort Walton Beach, Florida,
25-28 April 1995

Solid State Laser Programs at
Lincoln Laboratory

A. Sanchez

Diamond Cold Cathodes: Experiment
and Theory

M. W. Geis
J. C. Twichell
N. N. Efremow
K. E. Krohn
C. A. Marchi
T. M. Lyszczarz

High Definition
Information Exchange
Conference,
Arlington, Virginia,
30 April-3 May 1995

ORGANIZATION

SOLID STATE DIVISION

D. C. Shaver, *Head*
I. Melngailis, *Associate Head*
J. F. Goodwin, *Assistant*

A. L. McWhorter, *Fellow*
D. J. Ehrlich, *Senior Staff*
E. Stern, *Senior Staff*
C. L. Keast, *Staff*
D. Abusch-Magder, *Research Assistant*
T. M. Bloomstein, *Research Assistant*
J. T. Chiou, *Research Assistant*
J. P. Mattia, *Research Assistant*
N. L. DeMeo, Jr., *Associate Staff*
J. W. Caunt, *Assistant Staff*
K. J. Challberg, *Administrative Staff*

SUBMICROMETER TECHNOLOGY

M. Rothschild, *Leader*
T. M. Lyszczarz, *Assistant Leader*
L. H. Dubois, *Senior Staff*[†]

Astolfi, D. K.	Horn, M. W.
Craig, D. M.	Kunz, R. R.
DiNatale, W. F.	Maki, P. A.
Doran, S. P.	Palmateer, S. C.
Efremow, N. N., Jr.	Reinold, J. H., Jr.
Forte, A. R.	Sedlacek, J. H. C.
Geis, M. W.	Stern, M. B.
Goodman, R. B.	Twichell, J. C.
Hartney, M. A.	Uttaro, R. S.

QUANTUM ELECTRONICS

A. Sanchez-Rubio, *Leader*
T. Y. Fan, *Assistant Leader*

Aggarwal, R. L.	Jeys, T. H.
Cook, C. C.	Kelley, P. L. [‡]
Daneu, V.	Le, H. Q.
DeFeo, W. E.	Ochoa, J. R.
DiCecca, S.	Zayhowski, J. J.
Dill, C., III	

ELECTRONIC MATERIALS

B-Y. Tsaur, *Leader*
D. L. Spears, *Assistant Leader*

Chen, C. K.	Krohn, L., Jr.
Choi, H. K.	Manfra, M. J.
Connors, M. K.	McGilvary, W. L.
Finn, M. C.	Nitishin, P. M.
Golovchenko, P. A.	Pantano, J. V.
Harman, T. C.	Paul, S. A.*
Herrmann, F. P.	Turner, G. W.
Iseler, G. W.	Wang, C. A.

HIGH SPEED ELECTRONICS

M. A. Hollis, *Leader*
E. R. Brown, *Assistant Leader*
R. A. Murphy, *Senior Staff*

Bozler, C. O.	McIntosh, K. A.
Chen, C. L.	McMahon, O. B.
Goodhue, W. D.	Molnar, R. J.
Harris, C. T.	Nichols, K. B.
Lincoln, G. A., Jr.	Rabe, S.
Mahoney, L. J.	Rathman, D. D.
Mathews, R. H.	

* Research Assistant

[†] Intergovernmental Personnel Act assignment

[‡] Leave of absence

ELECTROOPTICAL DEVICES

R. C. Williamson, *Leader*
L. M. Johnson, *Assistant Leader*

Aull, B. F.
Bailey, R. J.
Betts, G. E.
Donnelly, J. P.
Groves, S. H.
Hovey, D. L.
Liau, Z. L.
Missaggia, L. J.
Mull, D. E.

O'Donnell, F. J.
Palmacci, S. T.
Poillucci, R. J.
Reeder, R. E.
Roussell, H. V.
Tsang, D. Z.
Walpole, J. N.
Woodhouse, J. D.

ANALOG DEVICE TECHNOLOGY

R. W. Ralston, *Leader*
T. C. L. G. Sollner, *Assistant Leader*
A. C. Anderson, *Senior Staff*
A. M. Chiang, *Senior Staff*

Arsenault, D. R.
Boisvert, R. R.
Brogan, W. T.
Denneno, J. M.
Feld, D. A.
Fitch, G. L.
Gleason, E. F.
Holtham, J. H.

Lyons, W. G.
Macedo, E. M., Jr.
McClure, D. W.
Murphy, P. G.
Oates, D. E.
Sage, J. P.
Seaver, M. M.
Slattery, R. L.

MICROELECTRONICS

E. D. Savoye, *Leader*
B. B. Kosicki, *Assistant Leader*
B. E. Burke, *Senior Staff*

Clark, H. R., Jr.
Daniels, P. J.
Doherty, C. L., Jr.
Dolat, V. S.
Donahue, K. G.
Donahue, T. C.

Felton, B. J.
Gregory, J. A.
Hotaling, T. C.
Johnson, K. F.
Lind, T. A.
Loomis, A. H.

McGonagle, W. H.
Mountain, R. W.
Percival, K. A.
Reich, R. K.
Thomas, J. W. §
Young, D. J.

§Staff Associate

1. ELECTROOPTICAL DEVICES

1.1 RELATIVE INTENSITY NOISE OF HIGH-POWER 1.3- μm InGaAsP/InP TAPERED DIODE AMPLIFIERS

High-power CW lasers are now widely used with external electrooptic intensity modulators for analog optical signal transmission. For these applications, low relative intensity noise (RIN) is a key requirement for realizing links with low noise figure and wide dynamic range [1]. Previously we described high-power InP-based tapered lasers operating at 1.3 μm with output power in excess of 1 W [2]. Here, we report preliminary noise measurements on tapered amplifier devices that show RIN levels as low as -164 dB/Hz at an output power of 360 mW. This low noise level is attractive for realizing compact and efficient high-power diode lasers for a wide variety of analog optical signal distribution systems.

The experimental arrangement showing the tapered laser amplifier design is presented in Figure 1-1. The amplifier has a 1-mm-long single-mode active waveguide section which serves as a preamplifier, followed by a 2-mm-long tapered gain region to provide a high-power output beam. The amplifier material was grown by atmospheric-pressure organometallic vapor phase epitaxy (OMVPE) and has three InGaAsP quantum wells under 1% biaxial compression and a double-step separate-confinement heterostructure region. The end facets of the amplifier were cleaved and antireflection coated with a quarter-wave layer of evaporated SiO_2 , resulting in reflectivity of approximately 1%.

The tapered amplifier was characterized by injecting light into the device from a diode-pumped Nd:YAG laser operating at 1319 nm. The beam power incident on the device was 40 mW, resulting in a coupled input power of roughly 15 mW. The RIN of the Nd:YAG laser is very low, under -170 dB/Hz, and thus output noise is dominated by that introduced within the amplifier. The input beam was polarized parallel to the plane of the amplifier chip. The amplifier output beam was approximately collimated and circularized by a microscope objective (0.5 numerical aperture) and a cylindrical lens. The beam passed through a 30-dB isolator to minimize back reflections into the amplifier and was then refocused onto an InGaAs photodetector. The detector output was amplified and then measured on an RF spectrum analyzer. For these preliminary measurements, careful spatial filtering of the output beam to eliminate sidelobes was not performed.

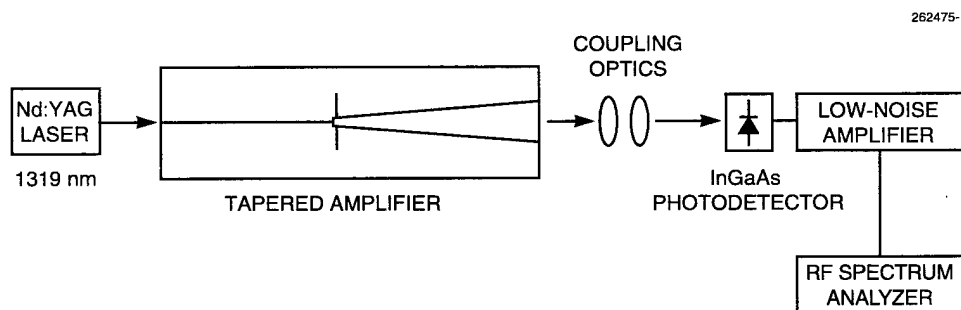


Figure 1-1. Schematic diagram of experimental configuration showing tapered amplifier device injected with light from diode-pumped Nd:YAG laser.

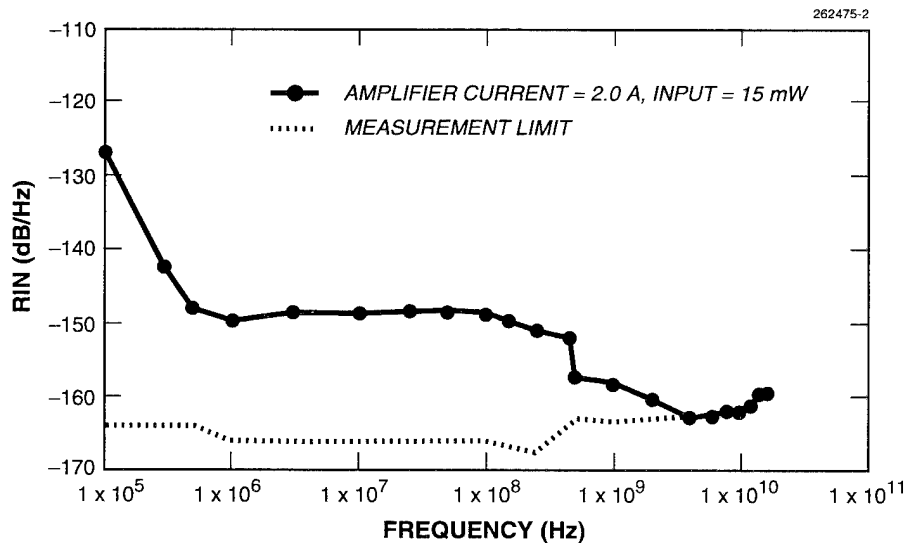


Figure 1-2. Measured relative intensity noise (RIN) spectrum of tapered amplifier operating at 1319 nm with output power of 360 mW.

The measured RIN spectrum of the amplifier output is shown in Figure 1-2 for an amplifier current level of 2.0 A and an output power level of 360 mW. As can be seen from these initial measurements, even without spatial and wavelength filtering, very low RIN of less than -160 dB/Hz is obtained between 2 and 10 GHz. For many analog link designs, this RIN level would result in minimal performance degradation as compared to that theoretically predicted with a noiseless source. Based on these results, it is envisioned that very compact high-power sources with low RIN can be realized by combining low-noise distributed-feedback diode lasers with high-power tapered amplifiers in a master-oscillator/power-amplifier configuration.

G. E. Betts	J. P. Donnelly
S. H. Groves	J. N. Walpole
F. J. O'Donnell	L. M. Johnson

REFERENCES

1. G. E. Betts, L. M. Johnson, C. H. Cox III, and S. D. Lowney, *IEEE Photon. Technol. Lett.* **1**, 404 (1989).
2. *Solid State Research Report*, Lincoln Laboratory, MIT, 1995:1, p. 1.

2. QUANTUM ELECTRONICS

2.1 CALORIMETRIC MEASUREMENT OF LOSSES IN 193-nm OPTICS

Optical components for use at excimer-laser wavelengths show appreciable transmission losses, of the order of a few percent, whose mechanisms and long-term changes are not entirely understood. A systematic study has been initiated, using specially fabricated samples which are irradiated by an ArF excimer laser. Figure 2-1 shows the setup used; the sample under test is rectangular in shape, all faces polished, and is supported by a thermoelectric module (TEM), which in turn is clamped on an aluminum block to provide good heat sinking. As long as the sample is close to room temperature, all heat dissipated in the sample, under steady state conditions, flows through the TEM. The TEM short-circuit current is measured by an operational amplifier; the output is proportional to the heat flow through the TEM, with a scale factor which can be easily calibrated. The TEM signal is therefore a direct indication of the absolute total loss in the sample. The transmitted laser power is monitored by a power meter.

The bottom surface of the sample is coated with an Al film, which has a high ($> 80\%$) reflectivity at ultraviolet through visible wavelengths. This eliminates most of the contribution to the signal due to scattered radiation, or fluorescence, hitting the TEM surface. The measurements performed in this configuration, therefore, are indicative of *absorption* losses suffered by the beam. If the sample side surfaces are blackened, radiation scattered through large angles, or reemitted as fluorescence, is also measured as heat flow through the TEM. This second measurement is therefore higher than the first and closer to the total (absorption plus scattering) loss. In principle, a more accurate measurement of the scattering losses including small-angle loss can be obtained by combining the absorption-only measurement with a transmission measurement utilizing the external power meter and suitable apertures. In practice, the accuracy is reduced owing to laser power fluctuations and power meter noise.

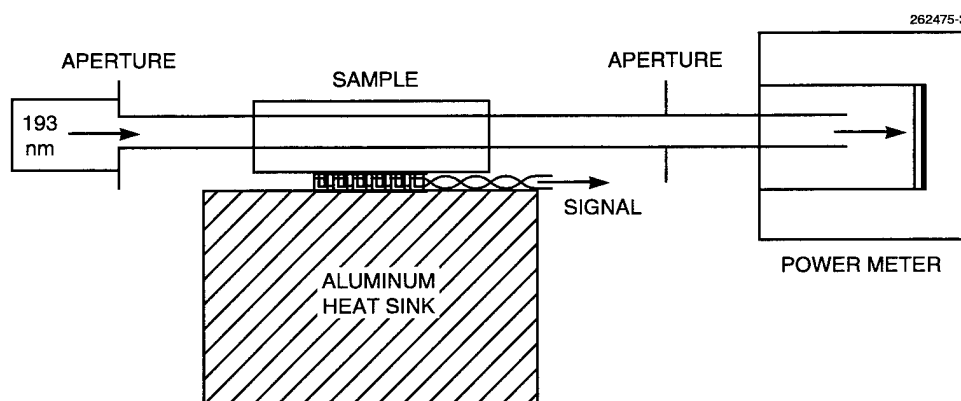


Figure 2-1. Setup for absorption measurements.

As mentioned, measurements have to be performed under steady-state conditions to be meaningful. Empirically, the step-function response for the sample dimensions used ($12 \times 22 \times 42 \text{ mm}^3$) is found to closely fit a simple exponential with a time constant of the order of 100 s; for repetition rates of a few hertz and above, the laser beam power is effectively CW if pulse-to-pulse variations are small. The excimer laser used (Lambda Physik LPX 210 type) can be run in a constant-energy mode with a stability of $\sim 1\%$ over 1 h. Rather than blackening the sample side walls to trap scattered radiation, it has been found easier to cover the sample with a loosely fitting aluminum shield, with the inner walls painted black. The cover can be quickly put in place or removed during the run, with only a minor change in the transient response time constant. Aside from possible initial aging effects, which are discussed below, absorption plus scattering and absorption only measurements can both be performed within 30 min or so.

Figure 2-2 shows data from a typical measurement run (Suprasil 1 fused silica) as a function of time. The initial part of the curve was recorded with the blackened Al cover resting on the sample. When a steady state had been reached after the initial turn-on transient, the cover was quickly removed, giving rise to a smaller transient owing to the removal of the scattering/fluorescence losses from the heat flowing through the TEM. The 193-nm power was monitored during the run by the power meter. By comparing readings with the sample in and out of the beam, a value for overall transmission is also obtained. From the known Fresnel loss at the input sample face, the absorption and total losses can then be expressed as a fraction of the beam power entering the sample. In the case of the sample in Figure 2-2, the total loss (from the steady-state level of the first part of the data) is 5.3%; the second part of the curve (no cover on the sample) yields a value of 4.7% for true absorption. The values given could be divided by the length of the specific sample used, to derive an absorption constant. However, preliminary measurements with varying sample lengths have shown the absorption to deviate appreciably from simple proportionality to length, implying that effects due to subsurface damage may be significant.

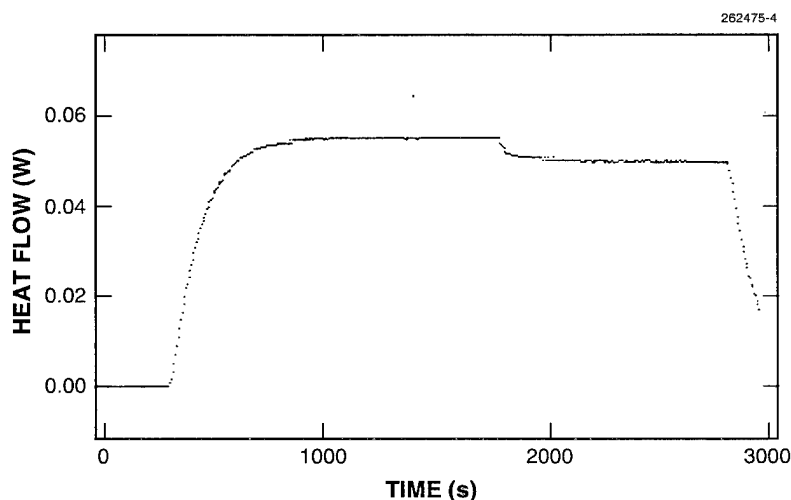


Figure 2-2. Flow through thermoelectric module as a function of time.

For some samples, a short-term aging or bleaching effect was observed. In the case of Figure 2-2, when the sample was *first* exposed to 193-nm radiation, the total loss initially reached a higher maximum value, corresponding to 6.3% of the beam power, followed by a decay to the lower, long-term steady-state value of 5.3% given above. The time for the loss to bleach to its final value was of the order of 1 h. Not all samples show this effect, and a correlation between the effect and the sample grade or source has not yet been determined.

V. Daneu

3. MATERIALS RESEARCH

3.1 InAsSb/InAlAsSb STRAINED QUANTUM-WELL DIODE LASERS EMITTING AT 3.9 μm

Mid-infrared (mid-IR) semiconductor diode lasers emitting between 3 and 5 μm would be very useful for highly sensitive detection of trace gases because many molecules including all hydrocarbons have strong absorption lines in this band. Lead-salt lasers, the only commercially available devices in this wavelength band, suffer from poor reliability. Thus, it is very desirable to develop mid-IR diode lasers from III-V alloys, because this material offers good metallurgical and thermal properties. Previously, InAsSb/AlAsSb double-heterostructure (DH) diode lasers with emission wavelength $\sim 3.9 \mu\text{m}$ have operated pulsed up to 170 K and CW up to 105 K [1]. Further performance improvement of the DH lasers should be possible by optimizing the laser structure and the growth parameters. Yet, the improvement may be somewhat limited because the characteristic temperature T_0 is only 20 K, presumably owing to Auger recombination. A better approach is to employ strained quantum-well (QW) structures because the strain can reduce the Auger recombination.

Recently, we have demonstrated the first strained QW diode lasers emitting in the 4- μm band by employing compressively strained InAsSb for the wells and tensile-strained InAlAs for the barriers [2]. However, these lasers emitting at $\sim 4.5 \mu\text{m}$ have operated pulsed up to only 85 K, probably because of nonuniform carrier distribution in the multiple QWs, which results in gain from only a few QWs and losses from the other wells. This nonuniformity is believed to be caused by a relatively large (85 meV) valence-band offset and a very small conduction-band offset. Much better performance was obtained from the same laser structure by optical pumping, which produces a much more uniform carrier distribution than electrical injection. Pulsed operation was obtained up to 144 K, with peak power at 95 K of 0.5 W. Here, we report improved InAsSb QW diode lasers emitting at $\sim 3.9 \mu\text{m}$ by employing InAlAsSb barriers, which provide a much larger conduction-band offset than InAlAs. The InAsSb/InAlAsSb QW lasers have operated pulsed up to 165 K and CW up to 123 K. The maximum power obtained at 80 K is 30 mW/facet. The value of T_0 has been increased to 30 K.

Figure 3-1 shows the calculated conduction- and valence-band offsets between $\text{InAs}_{0.85}\text{Sb}_{0.15}$ and InAlAsSb with a fixed tensile strain of 5×10^{-3} as a function of Al content. It was assumed that the valence-band position for the quaternary compound is a linear combination of values for binary compounds. The band-offset values for the binaries were taken from Tsou et al. [3], and the effect of strain on the band offset was calculated using the perturbation theory [4]. The valence-band offset increases very gradually with the Al content, while the conduction-band offset increases rapidly. For an Al content of 0.1, the conduction- and valence-band offsets are 85 and 55 meV, respectively.

The laser structures were grown on (100)-oriented *n*-GaSb substrates by molecular beam epitaxy [5]. The laser structure consists of the following layers: 1- μm -thick *n*-GaSb buffer, 3- μm -thick *n*- $\text{AlAs}_{0.08}\text{Sb}_{0.92}$ cladding, active region consisting of ten 15-nm-thick $\text{InAs}_{0.85}\text{Sb}_{0.15}$ active wells and eleven 30-nm-thick $\text{In}_{0.9}\text{Al}_{0.1}\text{As}_{0.9}\text{Sb}_{0.1}$ barriers, 3- μm -thick *p*- $\text{AlAs}_{0.08}\text{Sb}_{0.92}$ cladding, and 0.05- μm -thick *p*⁺-GaSb cap. The number of wells was reduced from 15 for the InAsSb/InAlAs QW lasers reported

previously, to reduce nonuniform carrier distribution. To have an adequate optical confinement, however, thicknesses for the wells and barriers were increased to 15 and 30 nm, respectively. The growth conditions were not optimized, and some texture was observed during inspection of the surface using Nomarski optical microscopy. Double-crystal x-ray diffraction measurement of the laser wafer showed somewhat broad satellite peaks, indicating imperfections in the interface quality.

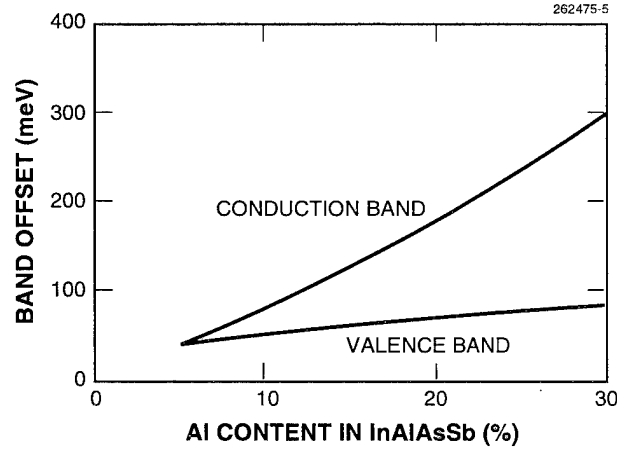


Figure 3-1. Calculated conduction- and valence-band offsets between $\text{InAs}_{0.85}\text{Sb}_{0.15}$ and InAlAsSb with fixed tensile strain of 5×10^{-3} as a function of Al content.

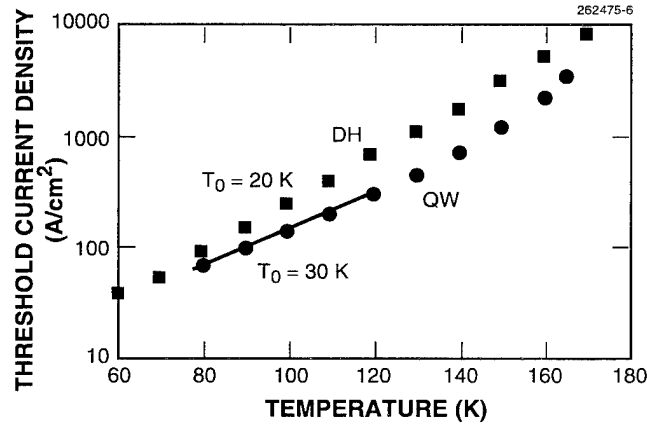


Figure 3-2. Pulsed threshold current density vs temperature of $100 \times 1000\text{-}\mu\text{m}$ strained quantum-well (QW) laser. Data for the best double-heterostructure (DH) laser at $3.9\text{ }\mu\text{m}$ are shown for comparison.

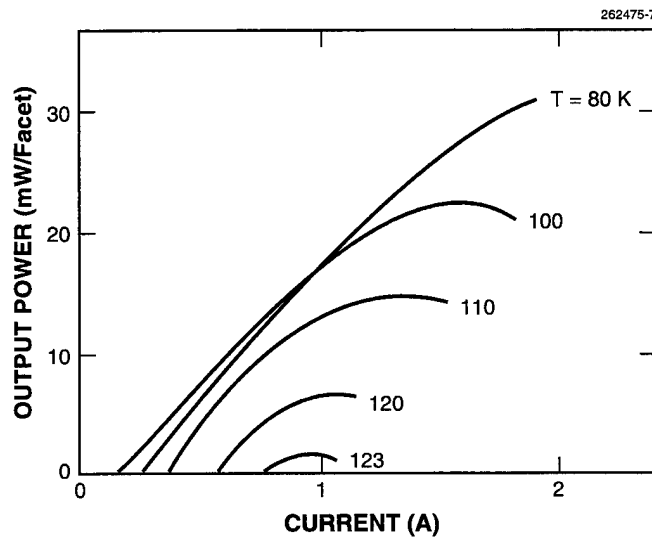


Figure 3-3. CW power vs current of $100 \times 1000\text{-}\mu\text{m}$ device at several temperatures.

Broad-stripe lasers $100\text{ }\mu\text{m}$ wide were fabricated by using SiO_2 patterning. Pulsed threshold current density J_{th} of a $1000\text{-}\mu\text{m}$ -long device with uncoated facets is plotted in Figure 3-2 for temperatures between 80 and 165 K. For comparison, data for the best DH lasers emitting at $3.9\text{ }\mu\text{m}$ are also plotted in the figure. At 80 K, the value of J_{th} for the QW device is 78 A/cm^2 . The value of T_0 up to 120 K is 30 K, which is larger than the 20 K observed for the DH lasers. Both the lower J_{th} and higher T_0 for the QW devices indicate that the Auger recombination, believed to be the limiting mechanism for $4\text{-}\mu\text{m}$ lasers, has been decreased by the employment of the strained QW structure. As the temperature is increased above 120 K, T_0 becomes smaller. At the maximum operating temperature of 165 K, the value of J_{th} is 3.5 kA/cm^2 .

Figure 3-3 shows the CW power vs current curves for the same device. The maximum power at 80 K is 30 mW/facet , which is much higher than 24 mW obtained at the same temperature for an InAsSb/AlAsSb DH laser with high/low facet coatings and mounted junction-side down [1]. The highest CW operating temperature is 123 K, which is higher than 105 K obtained for a $60\text{-}\mu\text{m}$ -wide DH device. The initial slope efficiency at 100 K is $\sim 0.05\text{ W/A}$, corresponding to a differential quantum efficiency of $\sim 16\%$. The slope efficiency at 80 K is smaller, but the reason for this is not clear. Many devices also showed self-pulsation below 100 K, which may be caused by traps in the material that are more active at lower temperatures.

H. K. Choi	W. L. McGilvary
G. W. Turner	M. K. Connors
D. R. Calawa	J. V. Pantano
J. W. Chludzinski	

3.2 *n*-AlGaSb AND GaSb/AlGaSb DOUBLE-HETEROSTRUCTURE LASERS GROWN BY ORGANOMETALLIC VAPOR PHASE EPITAXY

Previously, we reported growth of AlGaSb alloys by low-pressure organometallic vapor phase epitaxy (OMVPE) with tritertiarybutylaluminum (TTBAI), triethylgallium (TEGa), and trimethylantimony (TMSb) [6]. Alloys were grown over the whole composition range on GaSb substrates, and exhibited a mirror-smooth surface morphology and crosshatching owing to mismatch between the epilayer and the substrate. All layers exhibited *p*-type conductivity with a maximum hole concentration of $4 \times 10^{18} \text{ cm}^{-3}$, which is lower by a factor of 10 compared to layers grown previously [7], and consequently has more promise for *n*-type doping. Here, we report for the first time *n*-type doping of AlGaSb layers, and demonstrate room-temperature operation of AlGaSb/GaSb DH diode lasers.

Epitaxial layers were grown simultaneously on (100) GaSb and semi-insulating (100) GaAs substrates, misoriented 2° toward (110), in a vertical rotating-disk reactor operated at 150 Torr. TTBAI, TEGa, and TMSb were used as organometallic sources with diethyltellurium (DETe) diluted in H_2 (50 ppm) as the *n*-type doping source. For GaSb doping studies, the TEGa mole fraction was maintained at 2×10^{-4} , and the V/III ratio at 1.8. For AlGaSb layers, group III mole fraction was maintained at 1×10^{-4} and V/III ratio at 3.2. The DETe mole fraction was varied from 2.5×10^{-8} to 4×10^{-7} and the growth temperature was 550°C . AlGaSb epilayers were capped with a thin ($\sim 20 \text{ nm}$) GaSb layer to facilitate ohmic contact formation. The alloy composition of AlGaSb layers was determined by Auger electron spectroscopy based on GaSb and AlSb standards, and carrier concentration and mobility were determined from Hall measurements based on the van der Pauw method on etched cloverleaf structures. Carbon and Te concentrations were determined by secondary ion mass spectrometry (SIMS) based on ion-implanted GaSb standards.

The variation of electron concentration of GaSb and $\text{Al}_{0.4}\text{Ga}_{0.6}\text{Sb}$ layers on DETe concentration is shown in Figure 3-4. For GaSb layers, the electron concentration increases from $3.8 \times 10^{17} \text{ cm}^{-3}$ for a DETe mole fraction of 2.5×10^{-8} to a maximum of $\sim 1.1 \times 10^{18} \text{ cm}^{-3}$ for a mole fraction of 2×10^{-7} , after which it slightly decreases. Similar observations have been reported by Nakamura et al. [8] for DETe doping of GaSb layers. For $\text{Al}_{0.4}\text{Ga}_{0.6}\text{Sb}$ layers with comparable DETe doping concentrations, the electron concentration is lower by over an order of magnitude, which is partially a result of the higher residual hole concentration. Similarly, the electron concentration saturates for a DETe mole fraction in the range of $1\text{--}2 \times 10^{-7}$.

Although the residual hole concentration for $\text{Al}_x\text{Ga}_{1-x}\text{Sb}$ layers with $x > 0.45$ exceeds $1 \times 10^{18} \text{ cm}^{-3}$, these layers could be doped *n*-type, as shown in Figure 3-5 for $\text{Al}_x\text{Ga}_{1-x}\text{Sb}$ layers grown with a DETe mole fraction of 1×10^{-7} . For $x > 0.3$, the electron concentration decreases below 10^{17} cm^{-3} and was a minimum of $8 \times 10^{15} \text{ cm}^{-3}$ for $x = 0.75$, then increased to $3 \times 10^{16} \text{ cm}^{-3}$ for $x = 1$. The corresponding mobility, which has not been corrected for effects due to the G-L band proximity, initially decreases with x , and is a minimum at $x = 0.2$ (the G-L crossover point), but then increases toward the binary AlSb.

Carbon, Te, and O levels measured by SIMS are shown in Figure 3-6 for Te-doped AlGaSb layers grown under the same conditions as layers shown in Figure 3-5. The C level increases with x and is higher than the Te level for $x = 1$. Note that the incorporation of Te in AlGaSb is significantly less efficient than in GaSb. Since Te-doped AlSb layers exhibited *n*-type conductivity, the SIMS results suggest that some of the C may be interstitial and not electrically active. Oxygen levels are undesirably high at $\sim 10^{19} \text{ cm}^{-3}$, and are likely due to impurities in the organometallic sources.

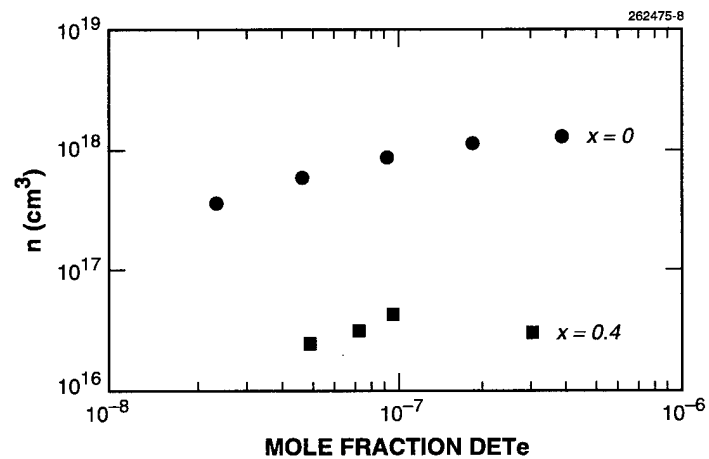


Figure 3-4. Electron concentration of Te-doped GaSb and $\text{Al}_{0.4}\text{Ga}_{0.6}\text{Sb}$ as a function of DETe mole fraction.

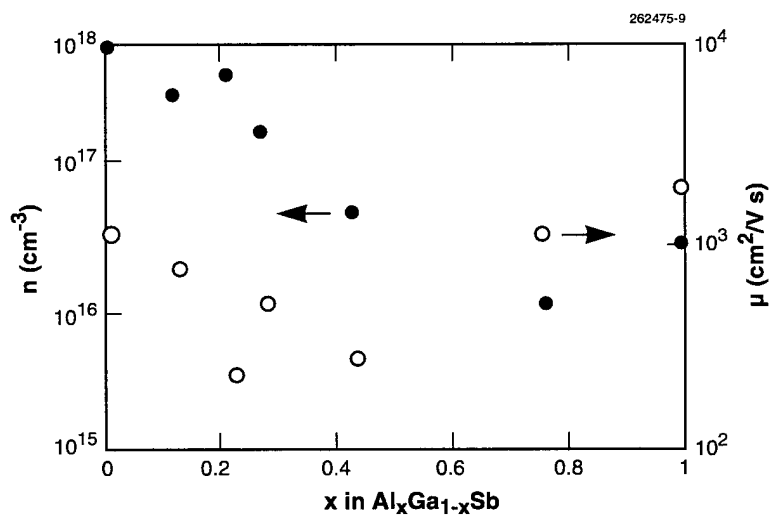


Figure 3-5. Room-temperature electron concentration and mobility of Te-doped $\text{Al}_x\text{Ga}_{1-x}\text{Sb}$.

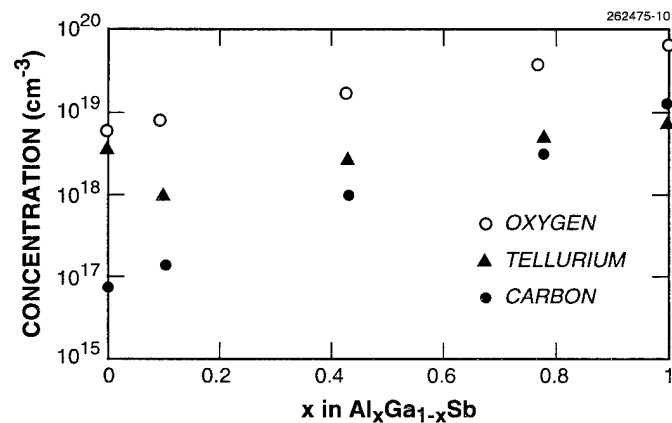


Figure 3-6. Carbon, tellurium, and oxygen levels in Te-doped $\text{Al}_x\text{Ga}_{1-x}\text{Sb}$ layers measured by secondary ion mass spectrometry.

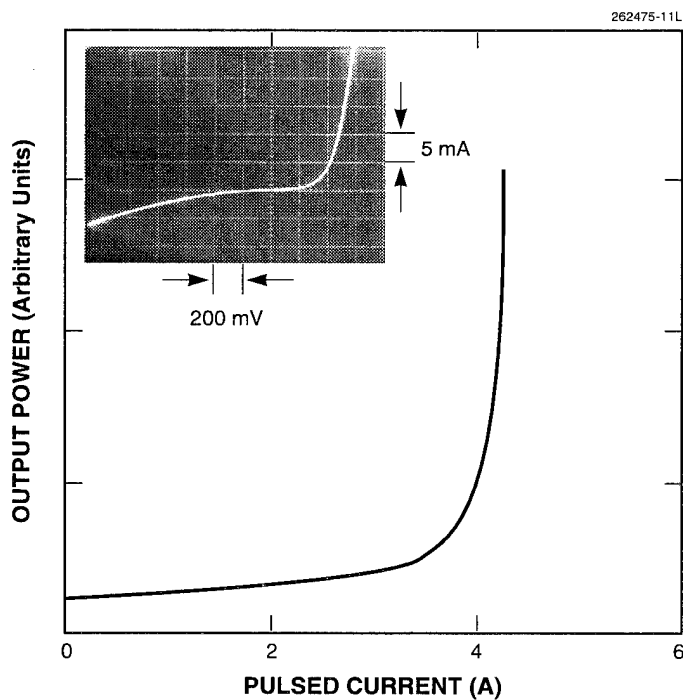


Figure 3-7. Pulsed power vs current for $100 \times 500\text{-}\mu\text{m}$ GaSb/AlGaSb DH laser emitting at $1.75\text{ }\mu\text{m}$. Inset shows I-V curve.

A lattice-mismatched DH diode laser consisting of 2- μm -thick $\text{Al}_{0.26}\text{Ga}_{0.74}\text{Sb}$ cladding layers and a 0.3- μm -thick GaSb active layer was grown on an *n*-GaSb substrate. Broad-area lasers were fabricated in the conventional manner [9], and devices 100 μm wide by 500 μm long were tested at room temperature with 400-ns pulses at a repetition rate of 1 kHz. The output power vs current is shown in Figure 3-7. The laser emitted at a wavelength of 1.75 μm with a pulsed threshold current density of 7.5 kA/cm^2 . The insert, which shows the I-V diode characteristics, indicates high leakage current as a result of dislocations associated with lattice-mismatched cladding layers. Although the performance of this initial demonstration of OMVPE-grown AlGaSb-based devices is inferior to similar structures grown by molecular beam epitaxy or liquid phase epitaxy, significant improvements are expected for lattice-matched heterostructure devices.

C. A. Wang W. L. McGilvary
M. C. Finn H. K. Choi

3.3 REACTOR DESIGN FOR IN-SITU OPTICAL MONITORING OF CHEMICAL VAPOR DEPOSITION REACTORS

In-situ monitoring of chemical vapor deposition systems can provide insights into complex growth mechanisms, and consequently could lead to improved control of growth processes and the resulting materials [10–12]. Raman scattering and spectroscopic ellipsometry are two useful techniques for obtaining quantitative information on semiconductor material properties, and can be employed during the growth process. A vertical rotating-disk reactor, which has been previously demonstrated for controllable and reproducible growth of highly uniform III-V heterostructures over a 5-cm-diam wafer [13], was modified to permit in-situ surface Raman scattering and spectroscopic ellipsometry.

Surface Raman scattering involves irradiating the substrate with a laser beam and collecting inelastically scattered light. The axis of the incident laser beam and collection optics should be as close as possible to the surface normal to access the desired Raman selection rules. The vertical rotating-disk reactor, shown in Figure 3-8, utilizes a mesh screen to ensure plug flow into the reactor, and was modified by incorporating an optical window at the center of the mesh. The diameter of the optical window is constrained by epitaxial growth nonuniformities and heterostructure grading that could occur if the unswept volume below the window is too large. In order to assess the effects of window diameter on growth, numerical simulations of the flow field and temperature were performed for the rotating-disk reactor operating under typical growth conditions (10-cm-diam quartz tube, H_2 carrier flow rate of 10 slpm, reactor pressure of 150 Torr, susceptor temperature of 650°C, and susceptor rotation rate of 400 rpm) for window radii of 1.27 and 2.54 cm. For the 1.27-cm-radius window, shown in Figure 3-9(a), the gas sweeps out the volume below the window with minimal change in temperature and flow fields compared to those computed without the window. Consequently, the epitaxial growth characteristics will be preserved. When the window radius is increased to 2.54 cm, shown in Figure 3-9(b), gas expansion results in a recirculation below the window which can lead to heterostructures with graded interfaces. Because of high gas diffusivity, layer uniformity is unaffected by the larger optical window.

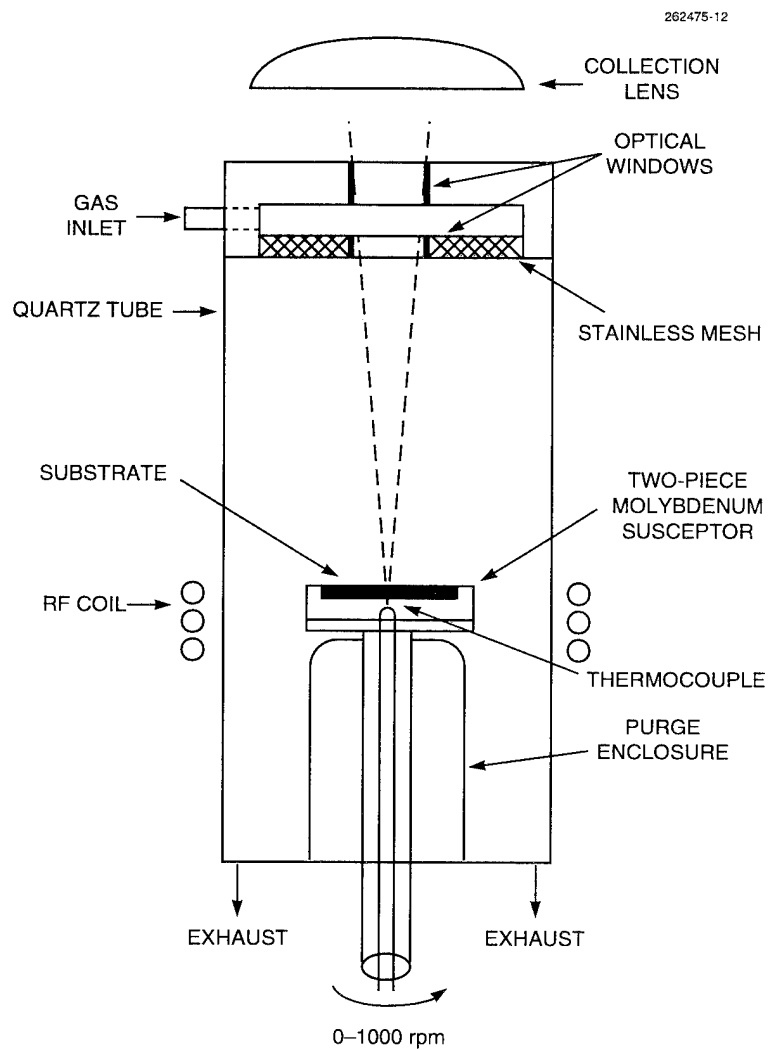


Figure 3-8. Vertical rotating-disk reactor design with top optical access for Raman scattering measurements.

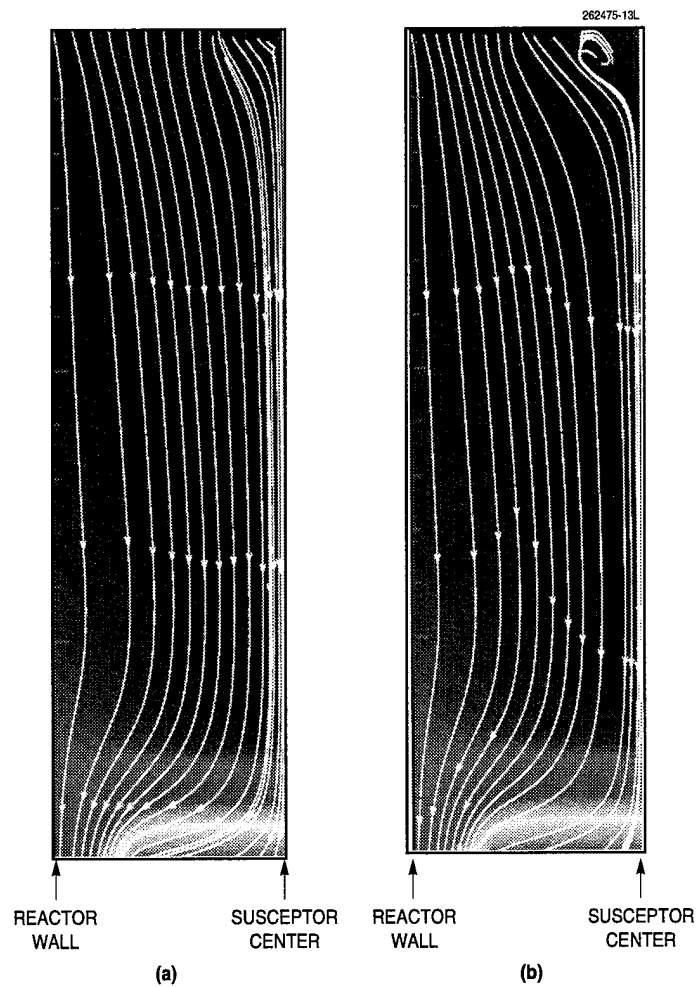


Figure 3-9. Flow patterns for (a) 1.27-cm-radius and (b) 2.54-cm-radius optical windows. The susceptor rotation rate is 400 rpm.

In the design for the growth reactor, the mesh screen was modified to incorporate a 3.8-cm-diam window mount which holds a 2.2-cm-diam clear aperture window. The distance between the mesh and the wafer surface is 15 cm, and therefore an incident/reflected angle of 4.2° can be accommodated with this window. To evaluate epitaxial uniformity with the modified mesh, a heterostructure that consists of 5-nm $\text{In}_{0.12}\text{Ga}_{0.88}\text{As}$ and 500-nm GaAs on a 5-cm-diam GaAs substrate was grown at a susceptor rotation rate of 450 rpm, and compared to the same structure grown with the original design. Thickness uniformity was determined by double-crystal x-ray diffraction (DCXD). Figure 3-10 shows the DCXD curves at three locations on the wafer radius for the structure grown with mesh modification. The Pendellosung fringes indicate high uniformity and abrupt layer growth. The DCXD data for the control sample are nearly identical.

The reactor tube design for spectroscopic ellipsometry, shown in Figure 3-11, permits optical access in the range between 68 and 77° from the substrate normal while minimally affecting the gas flow. A slit, 1.5 cm long by 0.3 cm wide, in the side of the quartz tube allows unperturbed propagation of the laser beam. A 4-cm-diam quartz tube is fused at a 10° angle to the main tube, and an optically flat window which also provides a vacuum seal is positioned in a precision-machined mount. To prevent deposition on the optical window, the side port is purged with carrier gas. The flow rate \mathcal{R} into the side port and through the slit must be balanced with the flow rate in the reactor tube, so that the flow through the annulus between the reactor tube and the susceptor is not perturbed, since growth rate uniformity can be affected.

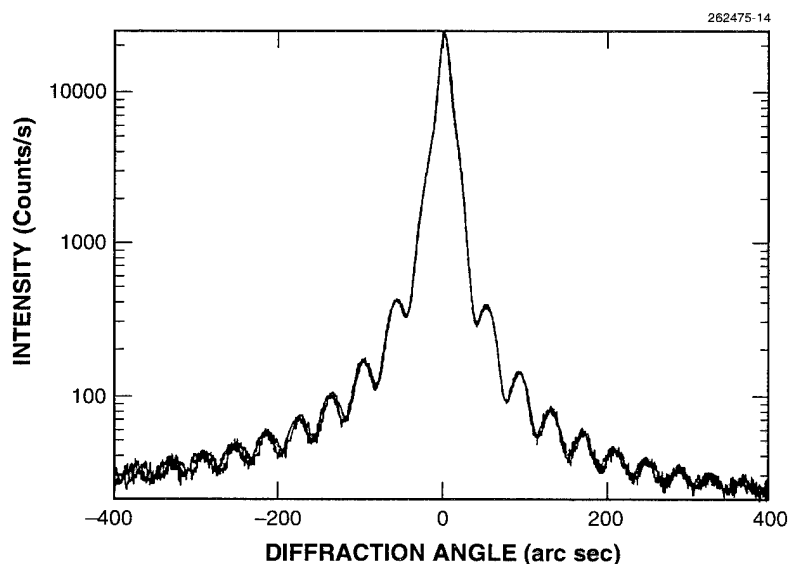


Figure 3-10. Double-crystal x-ray diffraction curves at three locations on wafer radius, showing high layer uniformity.

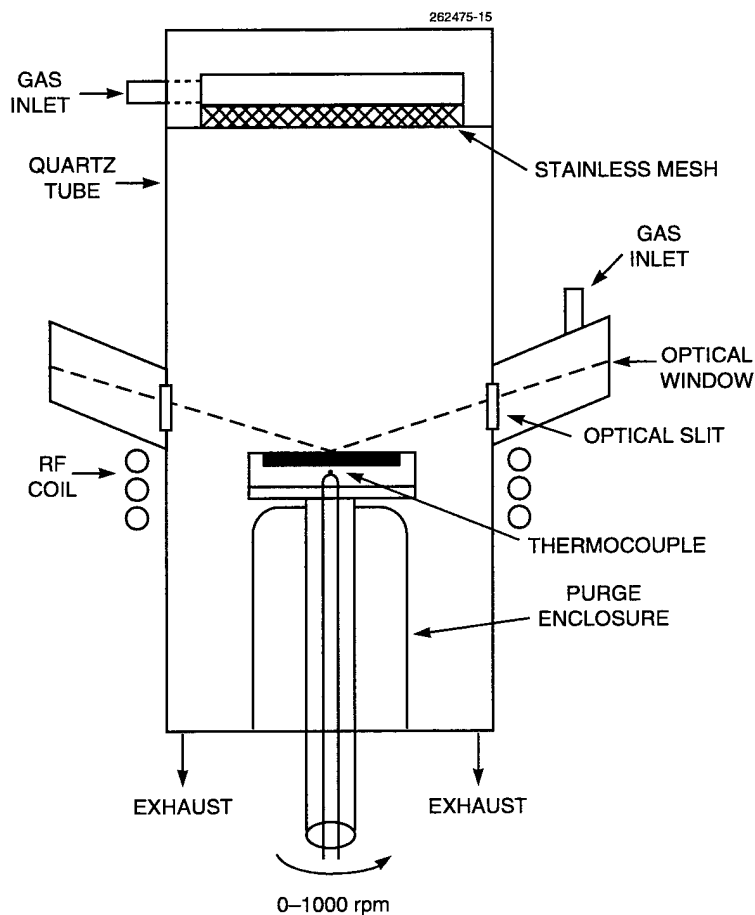


Figure 3-11. Vertical rotating-disk reactor design with side optical access for spectroscopic ellipsometry.

Flow visualization experiments were performed in a tube modified with one side port. Helium was used as the carrier gas at a flow rate of 10 slpm. TiO_2 particles were introduced into the gas flowing to the reactor tube but not into the gas to the purge port. The reactor was at room temperature and atmospheric pressure. A susceptor rotation rate ω equal to 90 rpm was used, which is just below the critical rotation rate for the onset of rotation-induced vortex flow. Although the reactor is operated at low pressure and elevated temperature during growth, these experimental conditions are expected to be applicable since the Reynolds number ($Re = VD_r/v$, where V is the average axial gas velocity, D_r is the diameter of the reactor tube [10 cm], and v is the gas kinematic viscosity) is independent of reactor pressure, and $\omega = 90$ rpm is chosen such that the rotational Reynolds number ($Re_\omega = \omega D_r D_s / 2v$, where D_s is the diameter of the susceptor [6.7 cm]) is similar to the value for 450 rpm that would be used for growth at 0.2 atm [14].

For $\mathcal{R} = 0$ sccm, the reactor gas infiltrates the side port, since the pressure in the reactor tube is greater than the pressure in the side port. In a growth experiment, this condition could result in deposition on the optical window, which would gradually reduce optical transparency. When $\mathcal{R} = 50$ sccm, the reactor flow is the same as the flow without the purge port, which indicates that the pressures in the main tube and side port are equally balanced. For $\mathcal{R} = 100$ sccm a void (due to the lack of smoke particles) adjacent to the slit was observed. As \mathcal{R} was increased above 100 sccm, the size of the void enlarged. At $\mathcal{R} = 300$ sccm the width of the void was about one-half the gap between the susceptor and the reactor tube wall, and at 550 sccm the width of the void equaled the gap width. Figure 3-12 shows the flow pattern observed for $\mathcal{R} = 300$ sccm. (Also incorporated in this test setup was a 3.8-cm-diam obstruction in the mesh at the top of the reactor inlet, which as can be seen did not affect the flow uniformity above the susceptor.) Based on these flow visualization experiments, we estimate that a purge flow rate between 50 and 100 sccm will be sufficient to prevent deposition on the optical window, and that purge rates less than 300 sccm should not affect growth uniformity.

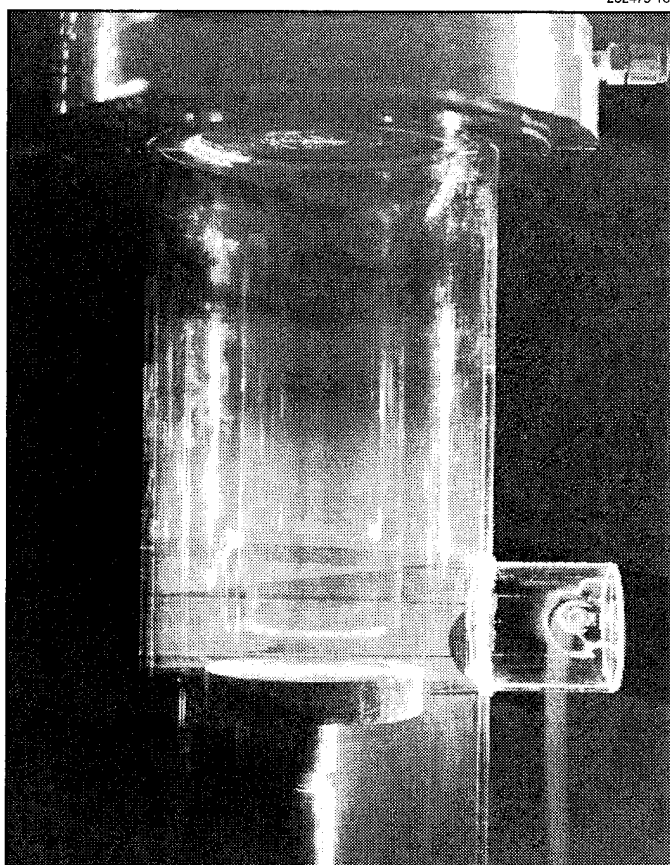


Figure 3-12. Flow visualization in reactor tube with modifications for in-situ monitoring by Raman scattering and spectroscopic ellipsometry.

Similar experiments were performed to evaluate the sensitivity of the purge flow rate on susceptor rotation rate. For $\omega = 0$ rpm, the width of the void equaled the gap width for a purge flow rate of 680 sccm, while for $\omega = 120$ rpm, a flow rate of 480 sccm was sufficient. These results are consistent with the fact that susceptor rotation imposes a pressure gradient that contributes to void formation.

C. A. Wang	J. W. Caunt
M. Zachariah*	K. F. Jensen*
D. R. Calawa	J. H. Reinold
D. L. Hovey	

REFERENCES

1. H. K. Choi, G. W. Turner, and Z. L. Liao, *Appl. Phys. Lett.* **65**, 2251 (1994).
2. H. K. Choi, G. W. Turner, and H. Q. Le, *Appl. Phys. Lett.* **66**, 3543 (1995).
3. Y. Tsou, A. Ichii, and E. Garmire, *IEEE J. Quantum Electron.* **28**, 1261 (1992).
4. N. G. Anderson, Ph.D. Thesis, North Carolina State University, 1988.
5. G. W. Turner, H. K. Choi, D. R. Calawa, J. V. Pantano, and J. W. Chludzinski, *J. Vac. Sci. Technol. B* **12**, 1266 (1994).
6. C. A. Wang, M. C. Finn, S. Salim, K. F. Jensen, and A. C. Jones, submitted to *Appl. Phys. Lett.*
7. E. T. R. Chidley, S. K. Haywood, R. E. Mallard, N. J. Mason, R. J. Nicholas, P. J. Walker, and R. J. Warburton, *J. Cryst. Growth* **93**, 70 (1988).
8. F. Nakamura, K. Taira, K. Funato, and H. Kawai, *J. Cryst. Growth* **115**, 474 (1991).
9. H. K. Choi and S. J. Eglash, *Appl. Phys. Lett.* **61**, 1154 (1992).
10. J. H. Olson and A. Kibbler, *J. Cryst. Growth* **77**, 182 (1986).
11. H. Sankur, W. Southwell, and R. Hall, *J. Electron. Mater.* **20**, 1099 (1991).
12. D. E. Aspnes, *IEEE J. Quantum Electron.* **25**, 1056 (1989).
13. C. A. Wang, S. Patnaik, J. W. Caunt, and R. A. Brown, *J. Cryst. Growth* **93**, 228 (1988).
14. C. R. Biber, C. A. Wang, and S. Motakef, *J. Cryst. Growth* **123**, 545 (1992).

*Author not at Lincoln Laboratory.

4. SUBMICROMETER TECHNOLOGY

4.1 OPTIMIZATION OF A 193-nm SILYLATION PROCESS FOR SUB-0.25- μ m LITHOGRAPHY

Top-surface imaged (TSI) resists have been developed as an alternative to bulk imaged resists [1] for high-resolution photolithography. These processes operate via area-selective in-diffusion of a silyl amine into a phenolic polymer to form a silyl ether. Once the silicon has been selectively incorporated, the latent image is developed in an anisotropic oxygen plasma etch. At 193 nm, the simplest TSI resist scheme is based on photocrosslinking of the polymer, followed by selective silylation of the unexposed areas [2]. Although chemical amplification schemes offer higher sensitivity [3] and may ultimately be the process of choice, the single-component direct crosslinking approach provides a simple platform for initial process evaluation of TSI at 193 nm.

The positive-tone 193-nm silylation resist process is illustrated schematically in Figure 4-1. A polyvinylphenol (PVP) resin is selectively crosslinked by exposure on a 0.5-numerical-aperture step-and-scan 193-nm optical lithography system. The sample is then treated with a silicon-containing vapor, dimethylsilyldimethylamine (DMSDMA), at a temperature of 90°C and a pressure of 25 Torr for 30–75 s. The uncrosslinked PVP areas incorporate a controlled amount of silicon, whereas the crosslinked areas do not. The wafers are then dry developed in a high-ion-density helicon plasma etcher in an oxygen-based plasma [4],[5]. The oxygen reacts with the silylated areas to form SiO_2 , which acts as an etch mask in the unexposed areas. The lithographic performance of this resist process depends upon the optimization of both the silylation and the etching.

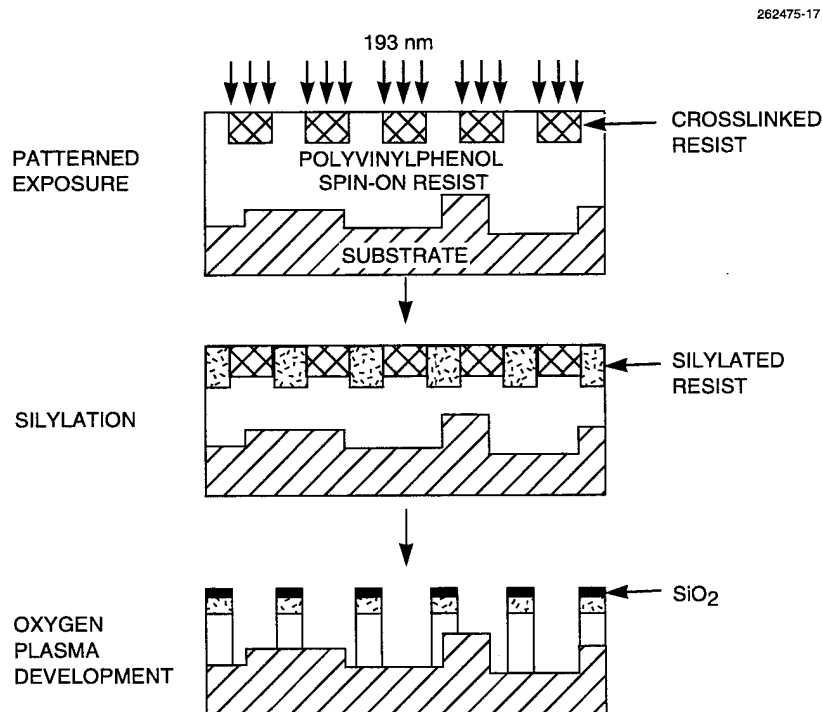


Figure 4-1. Schematic process flow for positive-tone 193-nm silylation process.

We chose to use DMSDMA to silylate PVP because of its high vapor pressure and small molar volume, which allows it to diffuse rapidly at low temperatures. This is useful for our single-component high-molecular-weight PVP resist which has a higher glass transition temperature T_g ($\sim 180^\circ\text{C}$) than many multiple-component chemically amplified TSI resists. One effect of this high T_g is slower diffusion rates which can be minimized by going to lower-molar-volume silylating agents. The larger-molecular-weight analogs trimethylsilyldimethylamine and trimethylsilyldiethylamine were also used to silylate PVP [6],[7]. The absolute diffusion/reaction rate is significantly faster for the smaller-molecule DMSDMA, while the contrasts for all three silylating reagents are comparable.

For a positive-tone process, the silylation mask shape is governed by the diffusion process of the silylating agent through the crosslinked latent image in the exposed resist film. The diffusion process and its dependence on feature size and type have been studied in detail previously [8]. We have demonstrated that the width of the silylated features is remarkably insensitive to defocus during the exposure, but the feature shape can undergo subtle changes that impact feature size during dry development. Nevertheless, the dry development conditions can be adjusted to compensate for these shape changes and thereby provide a large overall process window.

During the dry development, selectivity between the silylated and unsilylated resist is the variable that most dramatically affects exposure, focus, and etch process latitude as well as feature linearity. We have found that the chuck power is the etching parameter that produces the largest change in selectivity, from $\sim 160:1$ at 20 W to less than $20:1$ at 90 W. Selectivity is nearly independent of pressure (2–6 mTorr) and wafer temperature (30 to -70°C) at 2-kW source power, 50–75-W chuck power and 100-sccm O_2 . Again, we note a change at low pressure where the selectivity decreases from $30:1$ at 2 mTorr to $20:1$ at 0.5 mTorr, all other variables remaining the same. The selectivity at a given chuck power can be increased by increasing the flow rate or the source power. Modeling [9] of the silylation mask shape indicates that a selectivity greater than $20:1$ is required to obtain acceptable linewidth control with the 193-nm silylation resist. This requirement can be satisfied by lowering the chuck power. However, a lower limit on chuck power is imposed by the need to maintain a low lateral etch rate for profile control, as discussed below. Thus, an operating window on the chuck power is defined. For typical conditions of 2-kW source power, 2-mTorr pressure, 100-sccm O_2 , and -70°C , it is 35–75 W. Under these optimized process conditions, blanket wafer etch rate nonuniformity is less than $\pm 3\%$ over the central 85 mm of a 100-mm wafer.

In addition to adequate selectivity, it is necessary to optimize the resist profile. We used patterned trilayers with a SiO_2 hardmask to evaluate the effect of etch process parameters on resist profile under idealized silylation mask shape. A high degree of anisotropy is obtained by increasing the chuck power and decreasing the wafer temperature [10],[11]. Decreasing the wafer temperature from 30 to -70°C practically eliminates the isotropic etch component, while the vertical etch rate increases by $\sim 15\%$. An alternative way to reduce the lateral etch rate is to use a sidewall passivating gas such as SO_2 . However, the lateral etch rate is not eliminated but only reduced to ~ 20 nm/min, a value which causes a greater than 10% variation in $0.18\text{-}\mu\text{m}$ linewidths [12].

One of the main criteria for good lithographic performance is linearity, i.e., the ability to print a wide range of feature sizes and types within prescribed tolerances (e.g., $\pm 10\%$ of linewidth). Figure 4-2

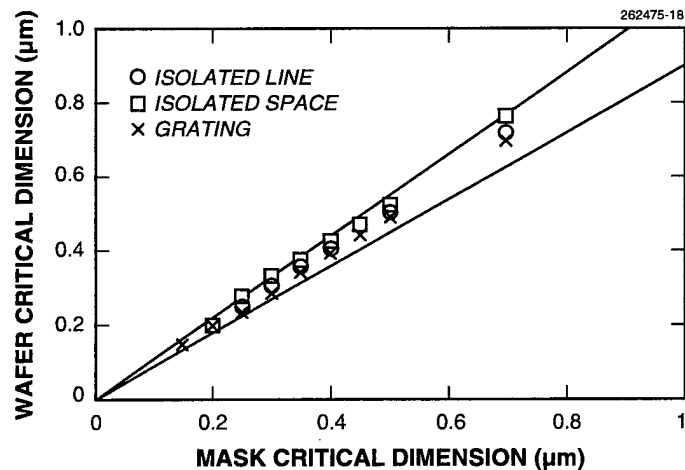


Figure 4-2. Silylation process linearity at best dose (100 dose units, $\sim 100 \text{ mJ/cm}^2$). The resist, 0.76- μm -thick polyvinylphenol (PVP) silylated with dimethylsilyldimethylamine (DMSDMA) at 90°C and 25 Torr for 60 s, was etched under optimized conditions (see Table 4-1) with a 100% overetch. The grating linearity is extended to 0.175 μm for a 30-s silylation time and 25% overetch. The two solid lines are the acceptable performance, i.e., $\pm 10\%$ deviations from the nominal feature size.

demonstrates the excellent linearity obtained with 193-nm TSI, using the process conditions listed in Table 4-1 for a 100% overetch and a 60-s silylation time (open field silylation depth 200 nm). For a wafer temperature of -70°C , linearity is maintained down to 0.20 μm for both a 25 and 100% overetch. For an etch temperature of 30°C , linearity is maintained down to 0.20 μm for a 25% overetch, but only to 0.30 μm for a 100% overetch. This is due to an increased isotropic etching component at 30°C . The nominal best dose for a 100% overetch is 20% lower than for a 25% overetch to enable more silylation, which compensates for the longer etch. The grating-to-isolated-line bias for a 60-s silylation time decreases from 30 nm for the 25% overetch, to 5 nm for the 100% overetch. For a 30-s silylation time the grating-to-isolated-line bias is reduced to 5 nm for a 25% overetch. The grating-to-isolated-line bias is determined by the difference in aerial images, resulting in different shapes of the silylation mask and its response to the dry development conditions. The preceding linearity data are for a fixed silylation time (60 s). Dense feature linearity was extended down to 0.175 μm for a 30-s silylation time using the process conditions in Table 4-1 and a 25% overetch. For longer silylation times (60–75 s) feature linearity could not be maintained below 0.25- μm features for these process conditions.

In addition to linearity, lithographic performance is also judged by the extent of the exposure and defocus process latitudes. Figure 4-3 is a plot of total exposure latitude vs feature size (gratings) for 30- and 60-s silylation times and a 25% overetch. For the smaller features the exposure latitude increases for the thinner silylated thickness. Note that even for features as small as 0.175 μm , exposure latitudes of at least 20% are obtained.

TABLE 4-1
Silylation Process Parameters in Sub-0.25- μm Lithography

Parameter	Conditions
Substrate	HMDS-treated silicon wafers
Resist	0.05–0.76- μm Polyvinylphenol
Post-apply bake	120°C, 60 s
Exposure	SVGL 193-nm step-and-scan, 0.5 NA
Mask	Binary Cr/SiO ₂ dark field
Dose (range, step)	27–225 mJ/cm ² , 10%
Focus (range, step)	–1.2 to 1.2 μm , 0.2 μm
Silylation	DMSDMA 90°C/25 Torr/30–75 s
Dry development	2-kW Source power, 75-W chuck power, 2-mTorr pressure, 100-sccm O ₂ , –70°C
Resist etch rate	1.6 $\mu\text{m}/\text{min}$
Selectivity	27:1 Open field

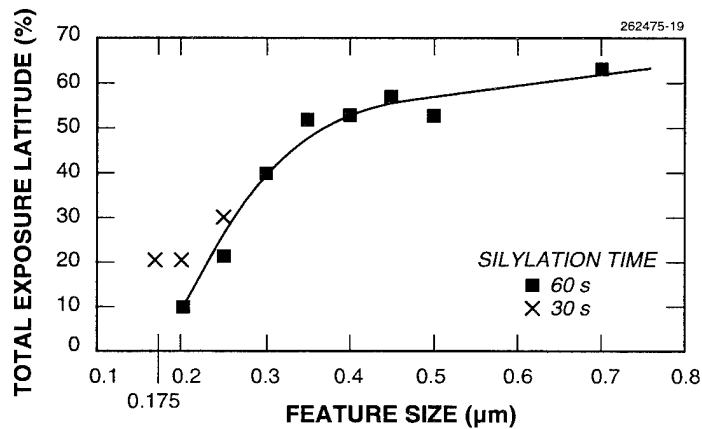


Figure 4-3. Total exposure latitude vs feature size for gratings ($\pm 10\%$ critical dimension). The resist, 0.76- μm -thick PVP silylated with DMSDMA at 90°C and 25 Torr for 30 and 60 s, was etched under optimized conditions (see Table 4-1) with a 25% overetch.

GRATINGS (μm)	K- FACTOR	DEFOCUS (μm)	DOSE UNITS						EXPOSURE LATITUDE
			100	110	121	133	146	161	
0.25	0.65	1.2							30%
		1.0							
		0.8	0.8	1.6					
		0.6							
		0.4							
		0.2			0.4	0.2			
		0							
0.20	0.52	-0.2							20%
		-0.4							
		0.8							
		0.6							
		0.4			1.0	1.0			
		0.2		0.2					
		0							
0.175	0.42	-0.2							20%
		-0.4							
		0.6							
		0.4							
		0.2				0.2	1.0	0.6	
		0							
		-0.2							

Figure 4-4. Experimental exposure-dose matrix for 0.25-, 0.20-, and 0.175- μm gratings ($\pm 10\%$ critical dimension). Each 193-nm dose unit corresponds to $\sim 1 \text{ mJ}/\text{cm}^2$. The resist, 0.50- μm -thick PVP silylated with DMSDMA at 90°C and 25 Torr for 30 s, was etched under optimized conditions (see Table 4-1) with a 25% overetch.

Figure 4-4 is a graphic representation of the experimental exposure-dose matrix for 0.25-, 0.20-, and 0.175- μm gratings for a 30-s silylation time and a 25% overetch. At best dose the depth of focus is 1.6, 1.0, and 1.0 μm , respectively. However, this maximum depth of focus is obtained at higher doses as the feature size decreases. Such behavior is in qualitative agreement with the aerial image simulation and corresponding exposure-defocus plots. The modeling predicts an 8.5% increase in best dose when the grating lines are reduced from 0.25 to 0.20 μm . This result is in close agreement with the 10% dose increase measured experimentally. The experimentally measured depth of focus values are less than those predicted theoretically. This is to be expected, since the simulation is only of the aerial image and does not take into account the silylation and etch steps. It should be noted that the data tabulated above are based on printed features that have near vertical sidewalls. Figure 4-5 illustrates a representative example of 0.20- μm silylated resist features after dry development.

S. C. Palmateer A. R. Forte
R. R. Kunz M. Rothschild
M. W. Horn

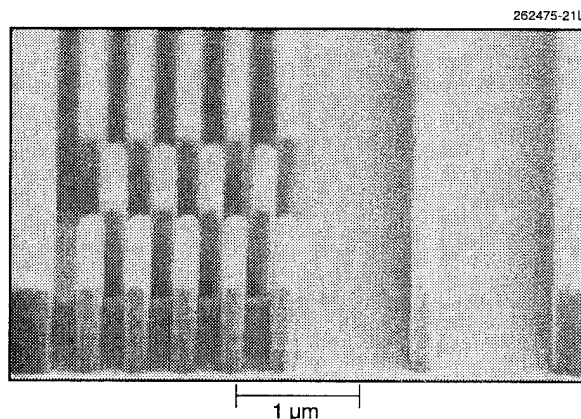


Figure 4-5. Scanning electron micrograph of 0.20- μm silylated resist features. The resist, 0.76- μm -thick PVP silylated with DMSDMA at 90°C and 25 Torr for 60 s, was etched under optimized conditions (see Table 4-1) with a 100% overetch.

REFERENCES

1. T. M. Wolf, G. N. Taylor, T. Venkatesan, and R. T. Kraetsch, *J. Electrochem. Soc.* **131**, 1664 (1994).
2. M. A. Hartney, M. Rothschild, R. R. Kunz, D. J. Ehrlich, and D. C. Shaver, *J. Vac. Sci. Technol. B* **8**, 1476 (1990).
3. M. A. Hartney and J. W. Thackeray, *Proc. SPIE* **1672**, 486 (1992).
4. N. Benjamin, B. Chapman, and R. Boswell, *Proc. SPIE* **1392**, 95 (1990).
5. M. W. Horn, M. A. Hartney, and R. R. Kunz, *Proc. SPIE* **1672**, 448 (1992).
6. M. A. Hartney, D. W. Johnson, and A. C. Spencer, *Proc. SPIE* **1466**, 238 (1991).
7. T. T. Dao, C. A. Spence, and D. W. Hess, *Proc. SPIE* **1455**, 257 (1991).
8. M. A. Hartney, *J. Vac. Sci. Technol. B* **11**, 681 (1993).
9. R. R. Kunz, M. A. Hartney, and R. W. Otten, Jr., *Proc. SPIE* **1927**, 464 (1993).
10. S. Tachi, K. Tsujimoto, and S. Okudaira, *Appl. Phys. Lett.* **52**, 616 (1988).
11. A. Bensaoula, A. Ignativ, J. Strozier, and J. C. Wolfe, *Appl. Phys. Lett.* **49**, 1663 (1986).
12. O. Joubert, C. Martinet, and J. Pelletier, *Proc. SPIE* **1803**, 130 (1992).

5. HIGH SPEED ELECTRONICS

5.1 FABRICATION AND MICROWAVE CHARACTERIZATION OF THIN-FILM PZT CAPACITORS

The multichip module (MCM) offers many advantages for ultra-high-speed electronic systems. In order to take maximum advantage of MCM technology, it is necessary to confront the fact that current switching transients generated by the integrated circuits (chips) cause rapid voltage fluctuations, or "noise," on the power and ground planes of the MCM. The traditional solution to this problem has been to employ discrete decoupling capacitors around each chip on the MCM. It is clear that materials with high dielectric constants would be desirable, since they would reduce the necessary area and volume dedicated to the decoupling capacitors. Furthermore, the ability to integrate decoupling capacitors to the greatest extent possible will dramatically affect the high frequency limits of a given MCM technology. Recently, thin-film ferroelectric capacitors have been proposed as a solution to this technical challenge [1],[2].

We report here on the fabrication of thin-film capacitors made from lead zirconate titanate (PZT). The PZT films with Zr/Ti molar ratios of 30/70, 52/48, and 70/30 represented rhombohedral, morphotropic phase boundary, and tetragonal compositions. The films were fabricated by the sol-gel spin-on technique at Pennsylvania State University. The preparation of the sol was based on a procedure reported earlier [3],[4]. Lead acetate trihydrate was dissolved in 2-methoxyethanol in a three-neck reaction flask, and refluxed under heat. To remove the water of hydration, refluxing was continued until the temperature of the vapors condensing in the still head reached that of the pure solvent. The dehydrated solution was cooled to room temperature. Titanium isopropoxide and zirconium *n*-propoxide were then added (inside a glove box) to levels that correspond to the targeted stoichiometry of the films. The resulting solution was refluxed for a few hours, and the byproducts volatilized at 125°C. The final concentration of the solution was adjusted by either the removal or addition of the solvent.

Thin films of the required thickness were obtained by a multistep spin-on procedure, with intermediate pyrolysis at each step at 400°C. The films were annealed at 700°C for 30 min for crystallization. Typically, films thicker than 0.5 μm were fabricated, since an earlier study [5] revealed a thickness dependence of the dielectric and ferroelectric properties of the PZT films for thicknesses < 3500 Å. Phase identification and microstructural investigations were carried out with a Scintag diffractometer and scanning electron microscope, respectively.

The ferroelectric films were formed on polished single-crystal sapphire substrates that were previously patterned with a 200-nm-thick evaporated platinum film. In addition to the platinum there was a 40-nm titanium adhesion layer between the platinum and the sapphire substrate. The platinum provides the best available back contact metal to the capacitors because it has minimal interaction with the ferroelectric film during annealing. Sapphire was chosen as the substrate because it also will have minimal interaction with the ferroelectric film.

After deposition the ferroelectric is removed everywhere except in the areas where the capacitors are to be formed using a photoresist mask and an etch composed of buffered HF, HCl and H₂O [6]. By using a photoresist lift-off process, the top titanium-gold layer is formed, which provides the front contact for the capacitors and also completes the coplanar waveguide test structure. The gold is evaporated to a

thickness of $0.5\ \mu\text{m}$, which allows a good contact to be made with the coplanar probes used in the measurement.

Measurements were performed on parallel-plate capacitors mounted in microwave-compatible test fixtures. The cross section and plan view structure of the capacitors is diagrammed in Figure 5-1. Several different sizes of capacitors with varying aspect ratios were fabricated to detect fringing effects or other geometry-dependent phenomena. Parasitic inductances in the coplanar waveguides caused the structures to resonate, and for the larger capacitors these resonances led to highly inaccurate results at frequencies above several hundred megahertz. However, the smallest capacitors measured $10 \times 10\ \mu\text{m}$ and yielded accurate results up to 10–15 GHz for the samples studied.

The electrical properties of several thin-film samples were investigated at the Mayo Foundation over a frequency range of 300 kHz to more than 10 GHz. To accomplish this measurement over such a broad frequency range, several different instruments were employed. At high frequencies the capacitance and dissipation were computed from scattering matrix data. The scattering parameters were measured with a Hewlett-Packard 4396 network analyzer from 10 MHz to 1.8 GHz, and with a Hewlett-Packard 8510C vector network analyzer from 100 MHz to 26.5 GHz. We were unable to approach their inherent resonant frequencies.

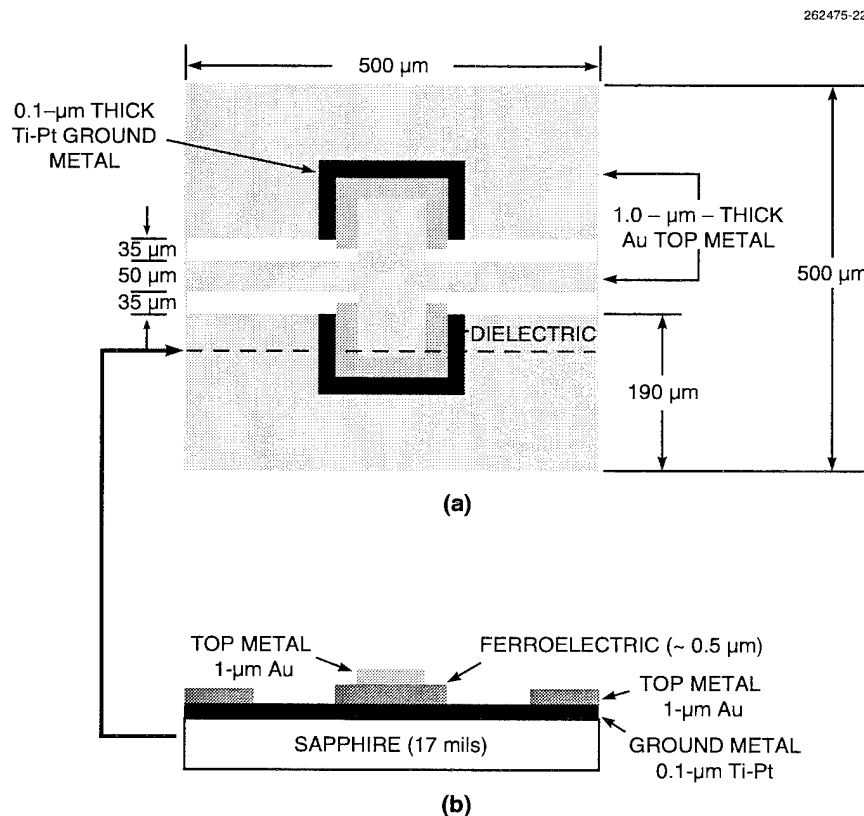


Figure 5-1. Top view of microwave coplanar waveguide structure for ferroelectric test chip.

TABLE 5-1
Voltage Dependence of Electrical Properties of 0.5- μ m
Thin-Film PZT at 5 GHz

Composition	Property*	Value at:		
		0 V	3 V	5 V
52/48	er	550	350	370
	D	0.14	0.125	0.11
30/70	er	600	580	520
	D	0.09	0.09	0.09
70/30	er	465	370	300
	D	0.15	0.12	0.10
*er is relative dielectric constant and D is dissipation factor.				

Our results demonstrate that the three samples all exhibit a decrease in dielectric response with increasing frequency. For the morphotropic and tetragonal phases a sharp rolloff in dielectric constant occurs at ~ 1.3 GHz. When the rolloff frequency is reached, the dielectric constant drops by 10–15%. The rolloff is attributed to the frequency of the alternating electric field exceeding the speed of domain wall movement. In other words the hysteretic polarization of the unit cells no longer contributes to the total polarization at ~ 1.3 GHz.

All three compositions of PZT studied exhibit a frequency-independent behavior of dielectric constant at frequencies above ~ 1 GHz. Therefore, there is an almost linear increase in the dissipation factor of the parallel-plate capacitors with respect to frequency. Each of the samples were measured at three separate bias voltages. All of the test instruments applied small signal analysis near these bias voltages. The effects of bias at 5 GHz on the material's dielectric constant and dissipation factor are depicted in Table 5-1.

We have demonstrated that the thin-film, sol-gel PZT retains a very high dielectric constant (over 500) at up to 15 GHz. The dissipation factor increases linearly with frequency over the 1-15 GHz range, achieving values as large as 0.25 for some samples.

C. M. Bozler

REFERENCES

1. D. Dimos, S. J. Lockwood, R. W. Schwartz, and M. S. Rodgers, *IEEE Trans. Components Packaging Manuf. Technol.* **18**, 174 (1995).
2. T. Garino, D. Dimos, and S. Lockwood, *Proceedings of the 1994 International Symposium on Microelectronics*, p. 179.
3. K. R. Udayakumar, J. Chen, S. B. Krupanidhi, and L. E. Cross, *Proceedings of the 1990 International Symposium on Applications of Ferroelectrics*, p. 741.
4. Y. Shimizu, K. R. Udayakumar, and L. E. Cross, *J. Am. Ceram. Soc.* **74**, 3023 (1991).
5. K. R. Udayakumar, P. J. Schuele, J. Chen, S. B. Krupanidhi, and L. E. Cross, *J. Appl. Phys.* **77**, 3981 (1995).
6. S. Mancha, *Ferroelectrics* **135**, 131 (1992).

6. MICROELECTRONICS

6.1 CHARGE-COUPLED-DEVICE DETECTION OF MICRO DISPENSED DNA HYBRIDIZATION ARRAYS

Sensitive detection of micro dispensed nucleic acids is needed for automating the method of DNA sequencing by hybridization [1]–[4]. Presently, x-ray film is the most commonly used tool in research environments for hybridization identification of DNA samples tagged using radioisotopes. However, microfabricated arrays require several hours of film exposure to distinguish matched from mismatched DNA samples, because of the low radioactivity levels associated with the very thin micro dispensed layers. To reduce the exposure time, charge-coupled devices (CCDs) were used in direct proximity to the hybridized arrays to detect the beta particles emitted from radioisotope-labeled samples. We present measured results, using the CCD and x-ray film for detection, taken on the first successful micro dispensed hybridization experiment.

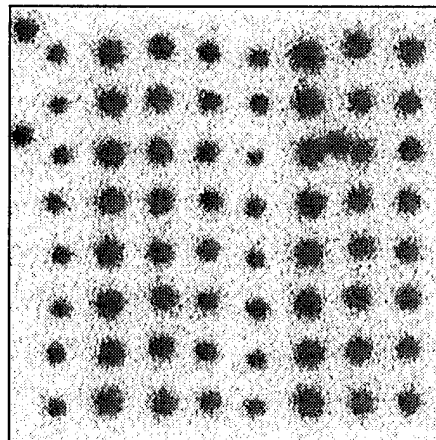
Experimental arrays were fabricated by micro dispensing dots of nucleic acid (called probes) onto a quartz substrate by a process similar to ink-jet printing [5]. Figure 6-1 shows the 8×8 dot arrangement of the probes with dot diameters of $\sim 100 \mu\text{m}$ and center-to-center spacing of $500 \mu\text{m}$. A particular array contained four columns, each column with a different probe. This pattern was repeated twice on the carrier substrate. Figure 6-2 gives the base sequence for the four different probes and the target DNA. The probes were nine bases long and had the same sequence except at one or two base locations. After fabrication of the probe array, a 9-mer target nucleic acid, containing the radioisotope label ^{35}S , was hybridized to the probe array. The target had an exact complementary match to probe T and was a mismatch to the other probes at one or two base sites. Figure 6-1 shows the room-temperature detection of the hybridized nucleic acid for three detection conditions.

Placement of the carrier substrates on the CCD for proximity imaging of beta particle emission is shown in Figure 6-3. The carrier substrate surface is separated by a few micrometers from the CCD imager surface. A 420×420 -pixel frame-transfer CCD imager (device name CCID7), operating at -70°C , was used to form the two-dimensional image of the radioactivity. In Figure 6-1, bright regions in the CCD image correspond to the highest levels of radioactivity. Already after 1 min of exposure on the CCD by the array, different activity levels for the four different probes could be quantitatively distinguished. The exact matched probe site had 1.3 times more signal than the most active mismatched probe and 5 times more signal than the least active mismatched probe; it should be noted that hybridization conditions were purposely adjusted to be of "low" stringency in order to visualize all the target-probe pairs.

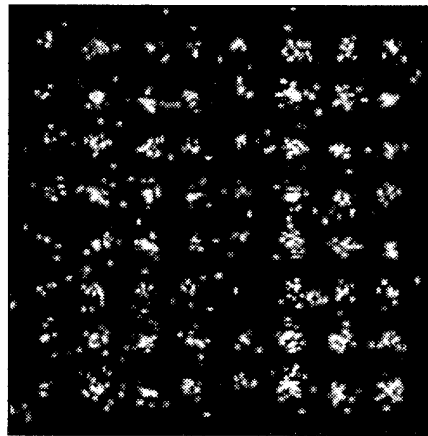
Figure 6-1 also shows the two-dimensional proximity image pattern created using x-ray film, where dark regions in the picture now relate to areas of high radioactivity. The exposure time to develop this image was about 8 h and is qualitatively comparable to the CCD image in Figure 6-1 that resulted after 6 1/2 min. Earlier calibration experiments indicate that the CCD should be approximately 1000 times more sensitive to the beta particle emitted from ^{35}S and are in agreement with this hybridization experiment.

R. K. Reich T. Powdrill*
D. B. Wallace* M. E. Hogan*

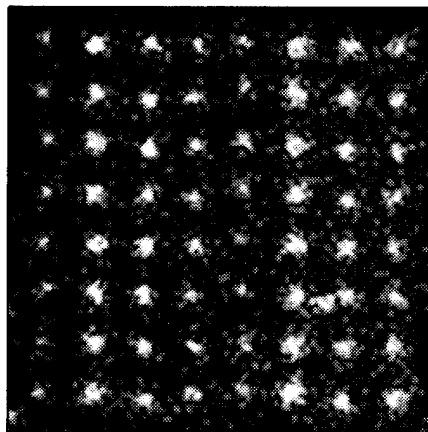
*Author not at Lincoln Laboratory.



X-RAY FILM
T = 8



CCD
T = 1 min



CCD
T = 6 1/2 min

Figure 6-1. Two-dimensional images formed by x-ray film and 420×420 -pixel charge-coupled device (CCD) imager after exposure to radioisotope-labeled hybridized array.

TARGET: 3'-ACCCCCTAG-5'*

PROBES:

- COLUMN 1: 5'-AGGGGGGATC-3A
(Single mismatch, position 1)
- COLUMN 2: 5'-CGGGGGGATC-3A
(Single mismatch, position 1)
- COLUMN 3: 5'-TGGGGGGATC-3A
(Perfect match)
- COLUMN 4: 5'-GAGGGGGATC-3A
(Double mismatch, positions 1 and 2)

* ^{35}S Label on solution – state target.

A = Amine site of surface attachment of probe.

Figure 6-2. Sequences used in micro dispensed hybridization experiment. Target sequence has ^{35}S on 5' terminus. Probes were linked to glass substrates through their 3' terminus employing epoxysilane chemistry and an amino linkage as previously described in Ref. 6.

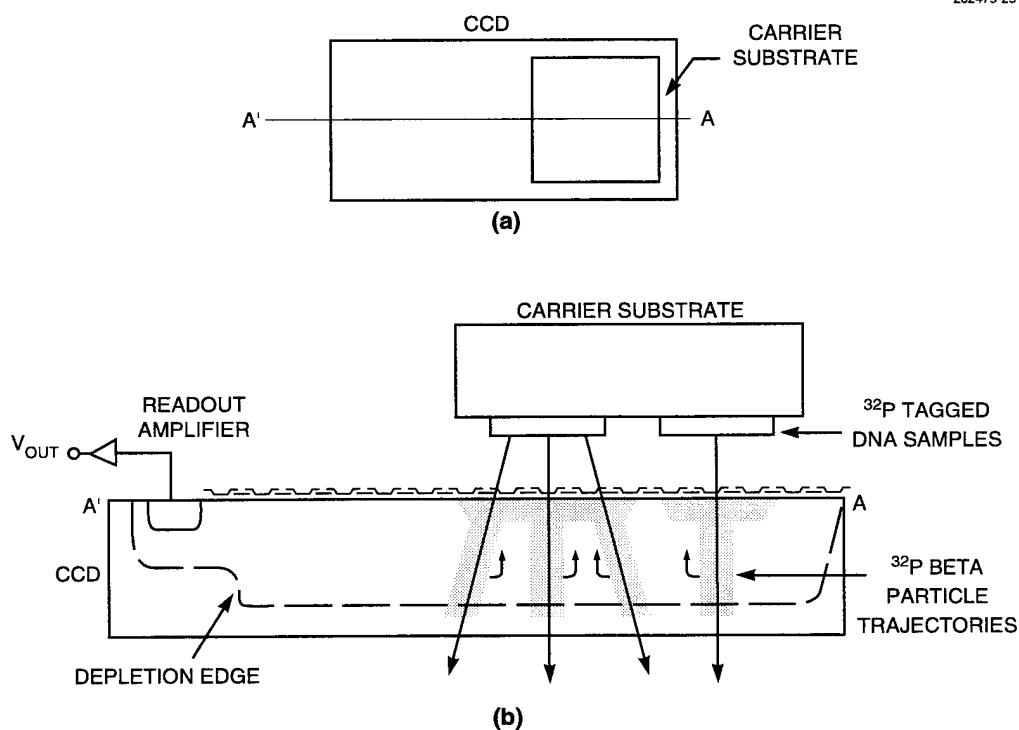


Figure 6-3. (a) Top and (b) cross-sectional views illustrating the placement of the carrier substrate containing the DNA samples relative to the CCD detector for proximity imaging of the beta particle emission.

6.2 FIRST IMAGING TESTS OF WAFER-SCALE CHARGE-COUPLED-DEVICE IMAGER

A large frame-transfer CCD imager which occupies an entire 100-mm silicon wafer [7] and a novel package for the device [8] have been described in previous reports. This device has been developed for use in the Air Force GEODSS (Ground-based Electro-Optical Deep Space Surveillance) system. Several of these imagers have been packaged and a detailed characterization of the device is currently in progress. In this report we describe the first imaging result of the large 1960×2560 -pixel device and of the small, high-frame-rate 32×32 -pixel devices located at the edges of the same die.

Figure 6-4 shows the image obtained by projecting a high-resolution transparency of a historic home in Lexington onto a front-illuminated 1960×2560 -pixel device. The temperature of the sensor was about -50°C , and the device was read out in the four-port mode. The boundaries of the four sectors of the device can be faintly discerned in the image as a result of the small gain and offset differences among the four video lines. The signal level averaged about half full well, and no cosmetic defects (bright pixels or dark pixels) are apparent, but at low signal levels a few isolated pixel defects become visible. Several imagers of this quality have been produced in the past year. The resolution of this device is sufficiently high that fine details in the image, such as the lettering on the plaque mounted on the right side of the house, can be read. Figure 6-5 shows this portion of the image expanded; the plaque describes the fate of the homeowner at the start of the Revolutionary War.

In addition to the 1960×2560 -pixel imager, there are two small 32×32 -pixel frame-transfer imagers located at the left and right edges of the device [7]. These are intended to be used as high-frame-rate photometers for measuring the light curve of tumbling space objects. We have tested this sensor by illuminating it with a pulsed light-emitting diode (LED) and operating the device at 1000 frames/s, which is the intended frame rate. A pinhole, illuminated by the LED, was imaged onto a few pixels of the device, and the pulse drive was synchronized to the CCD frame timing. Figure 6-6 shows a schematic of the test configuration and a photograph of the imager; the device in the figure is in the front-illuminated form, although the data shown here were taken on a back-illuminated version. The output video was digitized and stored, and the figure shows three of the frames of data. The first frame, just before the light pulse, shows only device noise, while the center frame shows the bright image of the pinhole. The subsequent image to the right shows no remnant trace (lag) of the spot.

B. E. Burke
H. R. Clark
T. A. Lind

262475-26L



Figure 6-4. Video image obtained from 1960 × 2560-pixel CCD imager.

262475-27L

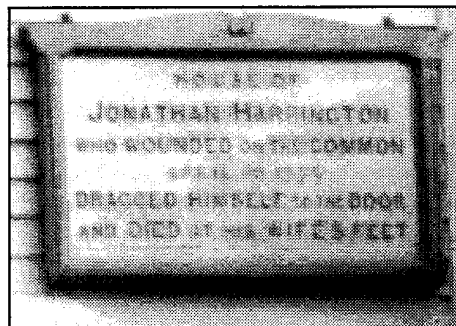


Figure 6-5. Expanded view of portion of image of Figure 6-4 containing plaque mounted on right side of house.

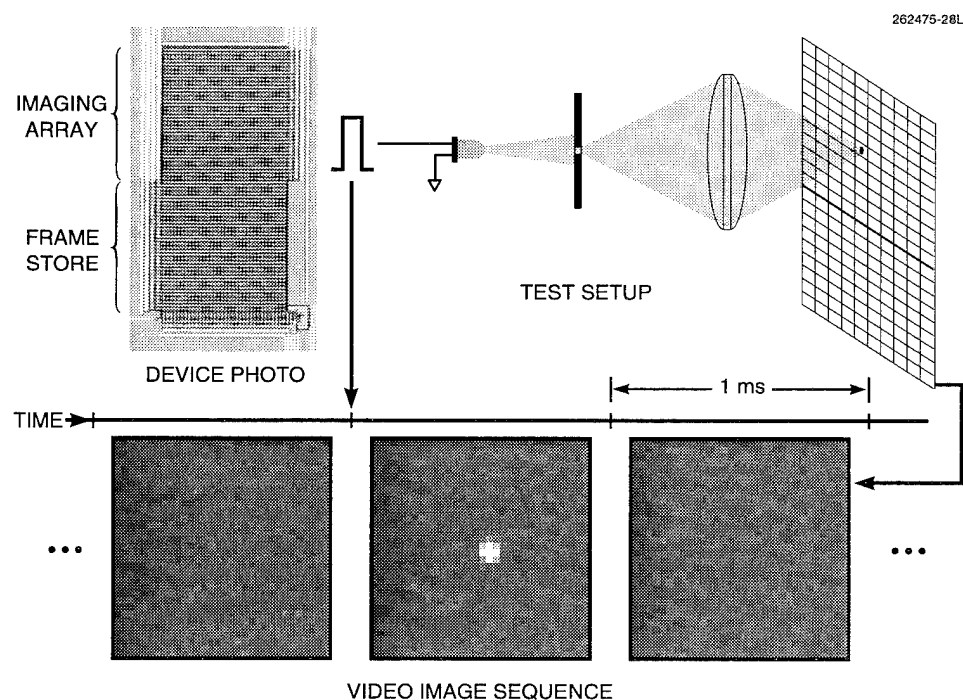


Figure 6-6. Test results on 32×32 -pixel imager located at edge of same chip as the large device and operated at 1000 frames/s. A pulsed light-emitting diode, pinhole, and lens are used to illuminate a small region of the device, and three frames of the output video are shown.

REFERENCES

1. R. Drmanac, I. Labat, I. Brukner, and R. Crkvenjakov, *Genomics* **4**, 114 (1989).
2. K. R. Kharpko, Yu. P. Lysov, A. A. Khorlyn, V. V. Shick, V. L. Florentiev, and A. D. Mirzabekov, *FEBS Lett.* **256**, 118 (1989).
3. W. Bains and G. C. Smith, *J. Theor. Biol.* **135**, 303 (1988).
4. E. Southern, Patent Application PCT IB 89/01114 (1988).
5. D. B. Wallace, ASME Publication 89-WA/FE-4 (1989).
6. J. B. Lamture et al., *Nucleic Acids Res.* **22**, 2121 (1994).
7. Solid State Research Report, Lincoln Laboratory, MIT, 1993:4, p. 39.
8. Solid State Research Report, Lincoln Laboratory, MIT, 1994:1, p. 35.

7. ANALOG DEVICE TECHNOLOGY

7.1 MICROWAVE FILTERS MADE FROM HIGH-TEMPERATURE SUPERCONDUCTORS WITH HIGH-POWER-HANDLING CAPABILITY

The very low microwave surface resistance of high-transition-temperature superconductors (HTS) makes HTS thin films obvious candidates for applications requiring microwave filters. In contrast with normal metals, however, the surface resistance of HTS thin films, at a given temperature, increases with the RF current circulating through them. Consequently, the insertion loss of devices built using these films depends upon the input power.

We have fabricated a number of HTS microstrip multipole filters with record power-handling performance. This was achieved by improvements in the HTS film quality as well as careful attention to the design of the filters. Figure 7-1 is a picture of one of these filters, a five-pole bandpass Tchebycheff microstrip filter, with 1% bandwidth, designed for a bandpass ripple of 0.1 dB. It was built using yttrium-barium-copper oxide (YBCO) thin films, deposited by cylindrical magnetron sputtering onto a 2-in.-diam 20-mil-thick LaAlO_3 substrate. The filter was designed to be centered at 2 GHz, since one of its envisioned uses is for new bands recently allocated for cellular telephone applications. In this design the forward coupling between adjacent resonators is due to the difference between odd- and even-mode propagation velocity in each coupled pair.

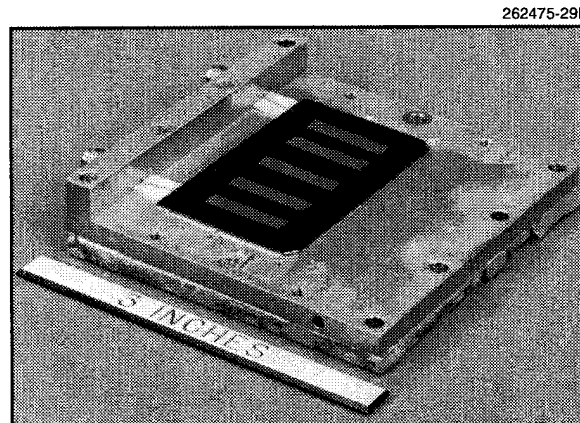


Figure 7-1. Photograph of high-temperature superconductive microwave filter built using thin films of yttrium-barium-copper oxide deposited on LaAlO_3 . The substrate is soldered to the package to ensure good thermal contact at low temperatures.

The design of the filter, achieved by a combination of analytical and numerical methods, emphasized the maximization of power handling. The individual resonators were made using approximately half-wavelength sections of 10- Ω microstrip lines. The use of wide lines increases their current-handling capability. We also chose a capacitively coupled structure for the input and output 50- Ω lines, since electromagnetic simulation of the current distribution in similar filters using a tap-coupled input/output structure showed strong current crowding at the intersection of the 50- Ω lines with the 10- Ω resonators. We used the following procedure to estimate the power-handling capability of this filter:

1. We measure the insertion losses and Q of a single 10- Ω YBCO resonator as a function of input power. We then use a circuit analysis based on a capacitively coupled parallel-LCR circuit to calculate the unloaded Q as a function of RF current in the resonator. A typical plot is shown in Figure 7-2.

2. We then synthesize the circuit equivalent of the desired filter using the procedure of Cohn [1]. This allows us to simulate the filter response using the computer program for circuit analysis, PSPICE. This simulation permits the calculation of the current in each resonator as a function of input power and frequency. Figure 7-3 shows how the current in each resonator of the filter of Figure 7-1 varies with the frequency for a 1-W input to the filter. Notice that the power handling of the filter will be limited by the currents circulating in the second resonator at the edge of the passband.

3. Since the unloaded Q of each resonator depends on the current circulating in that resonator, and all the currents are different, we must use a nonlinear model to calculate the insertion loss of the filter as a function of input power. The variation of Q for a single resonator with current I is well fit by the expression

$$Q = \frac{Q_0}{1 + aI^2 + bI^4} \quad , \quad (7.1)$$

with $Q_0 = 3.14 \times 10^4$, $a = 3.03 \times 10^{-3}$, and $b = 1.88 \times 10^{-6}$.

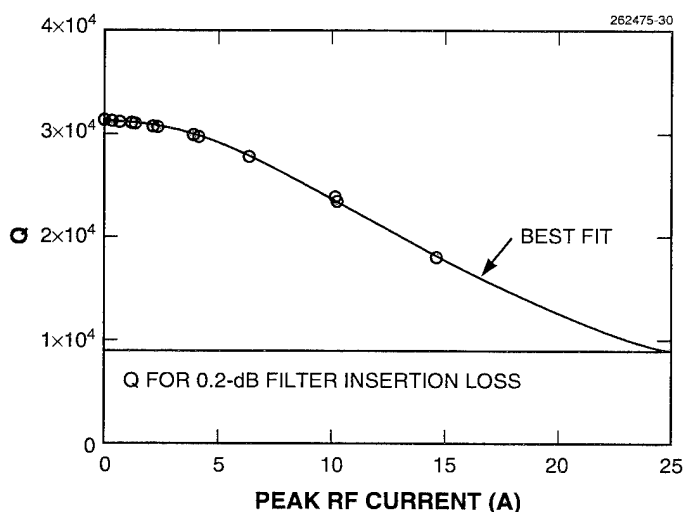


Figure 7-2. Variation of Q of 10- Ω microstrip resonator with peak RF current in the resonator. Measurements were made at 50 K.

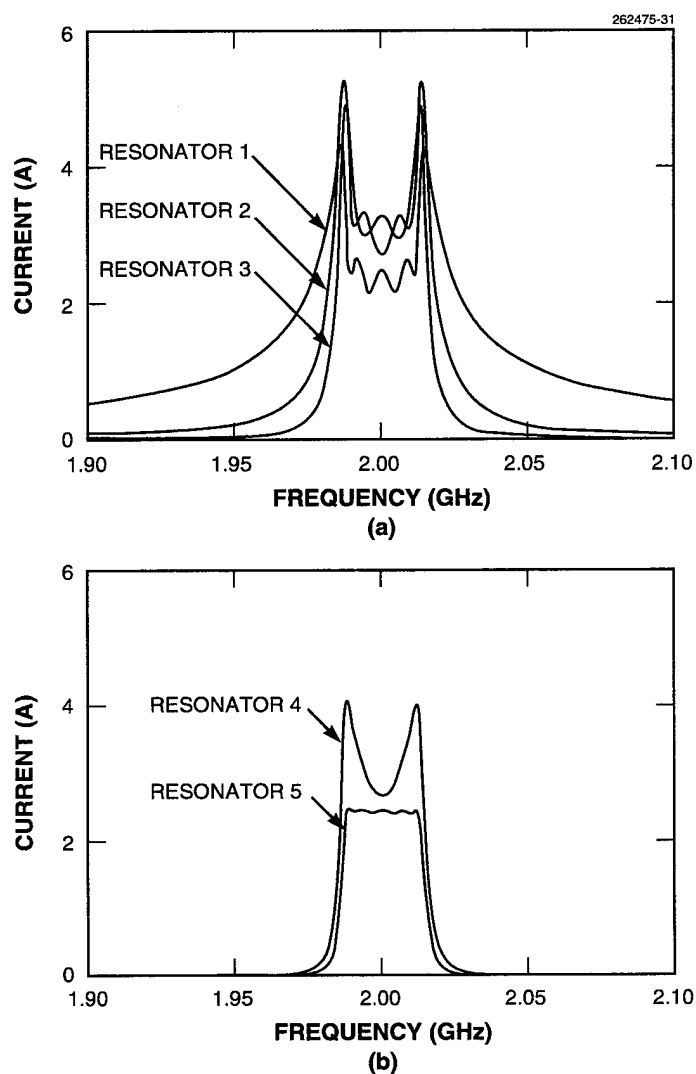


Figure 7-3. Calculated rms current in (a) resonators 1, 2, and 3 and (b) resonators 4 and 5 as a function of frequency for 1-W input to filter.

In a filter, except at very high input powers, the current in each resonator will be very close to sinusoidal in time, and this simplifies the analysis. The resonator losses, and hence the Q given above, may be simulated by a nonlinear resistor or, equivalently, by a voltage-dependent current source. We find that the expression for Q above leads to a current source that depends on the instantaneous resonator voltage as

$$i = 4.988 \times 10^{-6} \text{ V} + 2.015 \times 10^{-10} \text{ V}^3 + 1.499 \times 10^{-15} \text{ V}^5 . \quad (7.2)$$

This source can now be used in place of the resistors, which determine the Q of each section in the equivalent circuit of the filter, to simulate the insertion loss of the filter as a function of the input power. We calculated the insertion loss using the transient analysis capability of PSPICE. A transient analysis time of $2\ \mu\text{s}$ was sufficient to obtain the steady-state response of the filter.

The five-pole filter insertion loss calculated as a function of input power at two frequencies is shown in Figure 7-4. These frequencies correspond to the center of the band and to the band edge, where the maximum current is reached in resonator 2. We also show the measured insertion loss using a single tone at the center frequency. The agreement is good despite the fact that the insertion loss of the filter was measured for a temperature (45 K) slightly lower than that of the resonator of Figure 7-2 (50 K).

We show in Figure 7-5 the frequency response as a function of input power for the filter of Figure 7-1 measured at 58 K. As can be seen, the filter response at this higher temperature collapses suddenly near the edge of the band for input levels larger than 39 dBm (8.0 W). We believe this collapse is due to a thermal runaway situation, which is not included in the above calculation. Because, in a superconducting microstrip line, a large fraction of the RF current is crowded within a few penetration depths ($\sim 2000\ \text{\AA}$ for YBCO) of the line edges, and because, near the resonance for each resonator, the current distribution in the propagation direction is peaked in the center of the resonator, most of the power is being dissipated in a very small region. Consequently, this region will heat up, which in turn will cause the surface resistance to increase, which further increases the dissipated power. Above a certain input power level this will lead to a thermal runaway situation. At low temperatures this occurs for powers of tens of watts and has resulted in destruction of the filter.

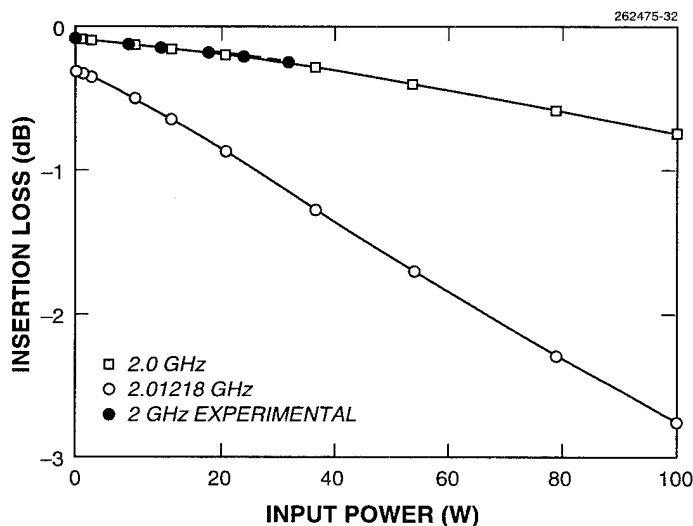


Figure 7-4. Calculated and measured insertion loss for filter of Figure 7-1. The calculations are based on Q measurements at 50 K. The insertion loss was measured at 45 K with a single-tone signal at the center of the band.

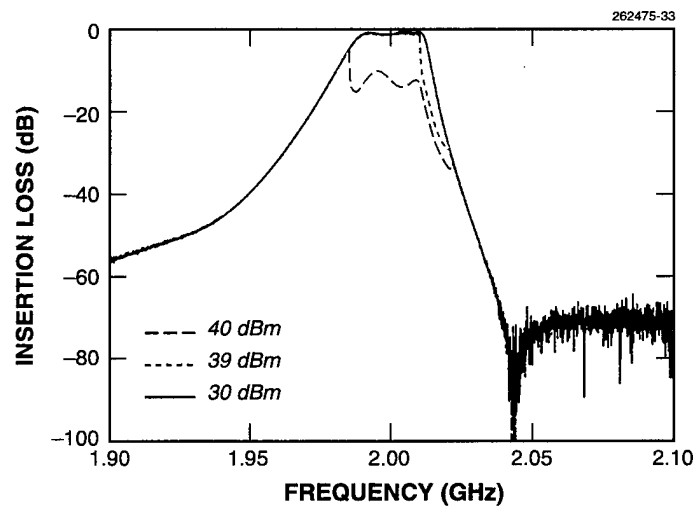


Figure 7-5. Measured frequency response of the filter as a function of the input power at 58 K.

To model this effect, the total thermal resistance between the patterned film and the cryocooler head must be known, and the variation of the Q of each resonator with temperature must be measured. Modeling of the thermal resistance of the package, including the current distribution in the resonators, and experimental verification of the model are currently under way.

A. C. Anderson

D. E. Oates

G.-C. Liang*

REFERENCE

1. S. B. Cohn, *Proc. IRE* **45**, 187 (1957).

*Author not at Lincoln Laboratory.

